Vol. 45 (2014) *ACTA PHYSICA POLONICA B* No 12

THE INITIAL STAGES OF HEAVY ION COLLISIONS[*]

François Gelis

Institut de Physique Théorique, CEA/DSM, 91191 Gif sur Yvette cedex, France

(Received November 12, 2014)

In this paper, I present the description of the early stages of heavy ion collisions at high energy in the Color Glass Condensate framework, from the pre-collision high energy nuclear wavefunction to the point where hydrodynamics may start becoming applicable.

DOI:10.5506/APhysPolB.45.2257
PACS numbers: 12.20.–m, 11.10.Hi, 11.15.Kc, 11.80.Fv

1. Heavy ion collisions

1.1. Reminder on QCD

Although they occupy only a tiny fraction of the volume of atoms (see Fig. 1), the atomic nuclei make up for most of the mass of ordinary matter. The protons and neutrons that are contained in nuclei each contain three valence quarks, that give them their quantum numbers. However, these quarks account only for a small part of their mass. Most of it comes from binding

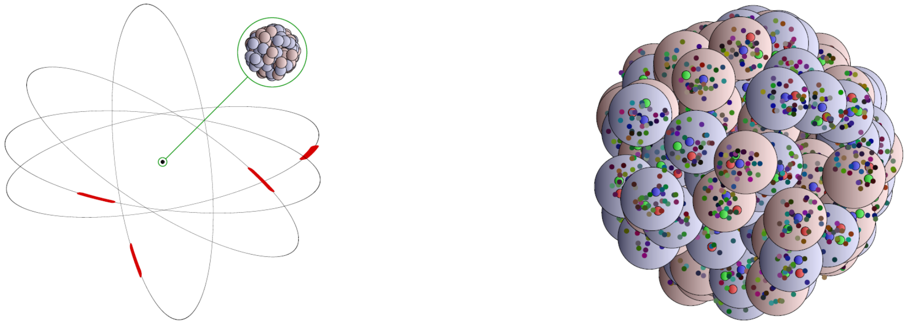

Fig. 1. Atoms and nuclei.

---

[*] Invited talk presented at the LIV Cracow School of Theoretical Physics "QCD Meets Experiment", Zakopane, Poland, June 12–20, 2014.

energy, *i.e.* from the cloud of gluons and virtual quark–antiquark pairs that surrounds the valence quarks. This predominance of binding energy in the mass of hadrons reflects a crucial property of the force that is responsible for the cohesion of hadrons and nuclei: this force becomes strong on distance scales comparable to the proton size, around 10^{-15} m. On the other hand, the measurements of structure functions in deep inelastic scattering experiments, first performed at SLAC in the 1960s, can be understood if one assumes that this force becomes weak on distance scales that are much smaller than the proton size.

The combination of these two properties paved the way to the development of Quantum Chromodynamics (QCD), as the microscopic theory that governs the interactions between quarks and gluons. On the surface, QCD is a gauge theory that resembles very much Quantum Electrodynamics. The matter degrees of freedom are spin 1/2 quarks, which interact by the exchange of vector particles, the gluons.

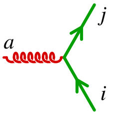

$$\sim \; g\,(t^a)_{ij}$$

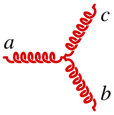

$$\sim \; g\,(T^a)_{bc}$$

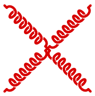

(1)

The quark–gluon coupling in QCD is very similar to the electron–photon coupling in QED, except that it has more "structure", since it involves a matrix of the fundamental representation of SU(3), t^a_{ij}. In this object, the index a (running from 1 to 8, the dimension of the SU(3) algebra) is the *color charge* of the gluon, and the indices i and j (running from 1 to 3, the dimension of the matrices in the fundamental representation of SU(3)) are the color charges of the incoming and outgoing quarks. The fact that the gluons themselves carry a color charge is the essential difference between QCD and QED, since it leads to novel interactions vertices that involve only gluons. These new interactions are a requirement of gauge symmetry, and can be derived from the following gauge invariant Lagrangian

$$\mathcal{L} = -\tfrac{1}{4}F^2 + \textstyle\sum_f \overline{\psi}_f (i\not{D} - m_f)\psi_f \,. \tag{2}$$

At the classical level, the only free parameters in QCD are the quark masses m_f and a coupling constant g. In the quantized theory, the coupling is usually traded for a scale[1] Λ_{QCD} that emerges from the renormalization of the coupling. This new scale arises in the running of the coupling constant $\alpha_{\text{s}} \equiv g^2/(4\pi)$. At one loop, this is given by

$$\alpha_{\text{s}}(E) = \frac{2\pi N_c}{(11N_c - 2N_f)\log\left(E/\Lambda_{\text{QCD}}\right)}\,, \tag{3}$$

---

[1] Note that, in the absence of quarks (or with only massless quarks), QCD is scale invariant at the classical level. Loop corrections induce a breaking of this scale invariance, which is the reason for the appearance of Λ_{QCD} in the quantized theory.

where E is the energy scale, N_c the number of colors and N_f the number of quark flavors. The main difference compared to QED, due to the self-interactions of the gluons, is the fact that the coupling becomes smaller at short distances, a property known as *asymptotic freedom*.

A related property of QCD is the long distance behavior of the interaction potential between a quark and antiquark. This can be calculated numerically in lattice simulations for heavy quarks (that are therefore static). This potential, shown in Fig. 2, behaves as a standard $1/r$ Coulomb potential at short distance, but increases linearly at large distance, in sharp contrast with QED. This leads to *color confinement*, that is the fact that free color charges cannot exist in Nature. Quarks only appear in color singlet bound states called hadrons, made of 3 quarks (baryons) or quark–antiquark pairs (mesons). The spectrum of these bound states can, in principle, be determined from first principles from the QCD Lagrangian, and it depends only on the quark masses and on the QCD scale $\Lambda_{\rm QCD}$. However, this dependence is non-perturbative and one has to use lattice simulations to perform these calculations. Presently, lattice calculations can reproduce the spectrum of light hadrons with an accuracy of the order of 5%, as illustrated in Fig. 3.

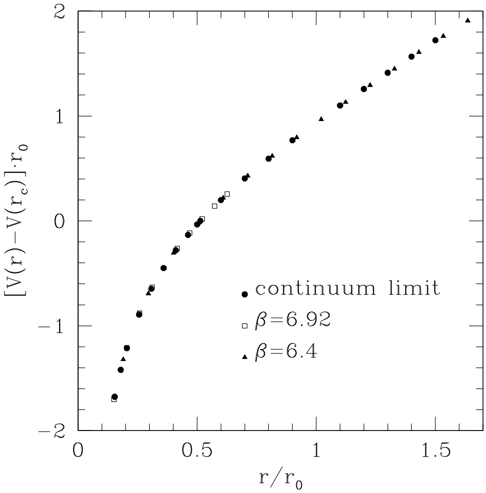

Fig. 2. Coulomb potential of a heavy quark and antiquark pair, from lattice QCD.

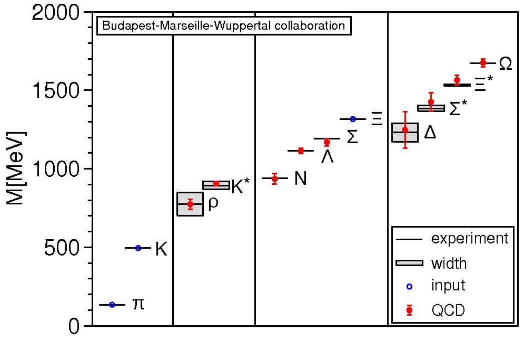

Fig. 3. Hadron spectrum from lattice QCD.

The QCD running coupling shown in Fig. 4 can also be viewed with a different spin: it suggests that if one squeezes many hadrons in a small volume, then the average inter-quark distance will be small and their interactions will be weak. In such a situation, the quarks would not be confined into individual hadrons, and would instead form a plasma made of deconfined quarks and gluons. This idea is substantiated by lattice calculations of the QCD partition function as a function of temperature, that indicate a rapid increase of the number of effective degrees of freedom at a temperature around 160 MeV [2]. This suggests that the relevant degrees of freedom are no longer the color singlet light hadrons (pions, kaons, ...) and have been replaced by quarks and gluons (that are more numerous because of the uncovered color degree of freedom).

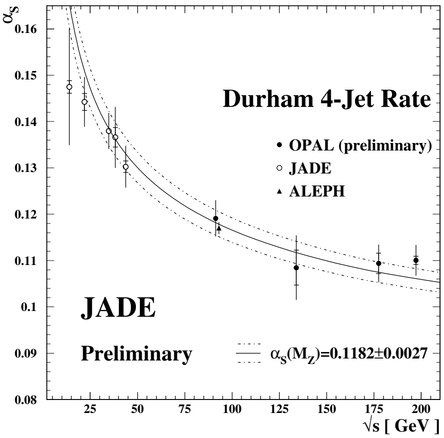

Fig. 4. Running coupling in QCD.

---

[2] This is for QCD with 3 light quark flavors. The transition temperature is higher for pure glue QCD.

1.2. Heavy ion collisions

Experimentally, the conditions of such a transition can be realized by colliding heavy nuclei at high energy. Such experiments are presently being performed by the RHIC (gold nuclei collided at 200 GeV) and by the LHC (lead nuclei collided at 5.5 TeV). Shortly after the impact of the two nuclei, the energy density reaches values that are more than ten times the normal nuclear matter density, well above the energy density at the deconfinement transition inferred from lattice calculations.

Such a collision, whose total duration is of the order of 10 fm$/c$, can be divided into several stages, as shown in Fig. 5. In this figure, we have also indicated what kind of tool one may employ for each of these stages. It turns out that macroscopic descriptions such as relativistic hydrodynamics are quite successful at describing the bulk evolution of the system. Somewhat surprisingly, the matter produced in these collisions seems to behave almost like a perfect fluid with close to no viscosity. A very small viscosity suggests that this matter is not the siege of strong dissipative processes that would rearrange its microscopic degrees of freedom.

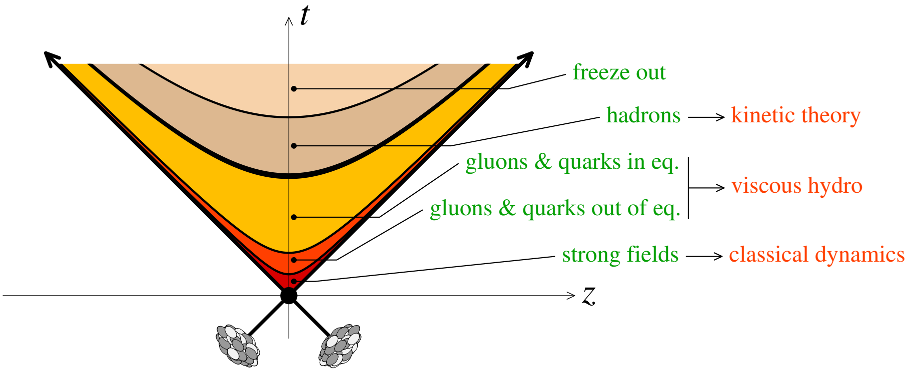

Fig. 5. Successive stages of a heavy ion collision.

In this paper, we will be chiefly interested in the beginning of the collision, up to the point where a hydrodynamical description may become plausible. We will adopt a weak coupling perspective, and we will try to follow a heavy ion collision in a description which is as closely related to QCD as possible. Indeed, in collisions at very high energy, the initial energy density is so large that the early stages of such a collision should be amenable to a weak coupling description, thanks to the asymptotic freedom of QCD. Note that a small viscosity, that could explain the success of hydrodynamics, can be obtained in the strong coupling limit, because the viscosity is inversely proportional to the scattering cross section of the quarks and gluons. However, it is also possible to get strong interactions at weak coupling, provided that the occupation number is inversely proportional to the coupling g^2. In this case, the coupling disappears from the scattering rate, and the system has many of the characteristics of a strongly coupled system.

2. Parton model

2.1. Kinematics

As discussed earlier, free quarks and gluons do not exist in normal nuclear matter. Instead they are confined into color singlet bound states, whose spectrum depends non-perturbatively on the parameters of the QCD Lagrangian. The same is true of the spectrum of the energy levels of a nucleus: it could, in principle, be derived from the underlying QCD dynamics, but this is even more complicated than in the case of light hadrons and, at the moment, far out of reach of lattice computations.

Does this mean that we should give up any hope of using QCD to describe collisions between such objects? Fortunately, the answer is no, *for collisions at sufficiently high energy*. The kinematics of such collisions is the key to overcome this difficulty. Let us consider first a nucleon at low energy (as seen when the observer is almost in the rest frame of the nucleon), shown in Fig. 6. In this cartoon, the thick lines represent the three valence quarks, and the horizontal axis represents time. Only gluon constituents are shown, not the sea quarks. In such a frame, the valence quarks appear to orbit with a period comparable to the proton size (they are ultrarelativistic). These quarks exchange gluons that provide the binding force, which also happens on scales of the order of the proton size. Moreover, the quarks and gluons can briefly fluctuate: for instance, a quark can temporarily become a quark+gluon state. The lifetime of these virtual states can be anything smaller than the proton size[3]. When studying reactions involving hadrons, one should compare the typical timescale of the collision (shown as a gray/blue strip in the figure) with the timescales of the internal dynamics of the nucleon. In collisions involving low energy hadrons, the hadron has a complicated inner

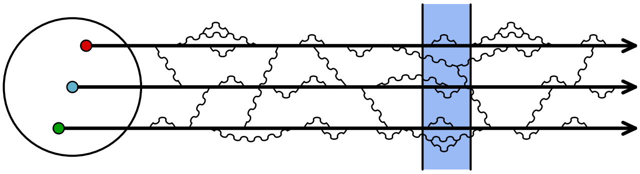

Fig. 6. Dynamics of the constituents inside a slow nucleon.

---

[3] But since QCD is a renormalizable theory, the physics of the strong interactions at hadronic energy scales does not depend on what may happen on much higher energy scales. Therefore, these fluctuations have essentially no relevance in hadronic physics.

dynamics on timescales comparable to the duration of the collision, which makes these collisions untractable in perturbative QCD.

Contrast this with what happens in a collision at very high energy. Although scattering amplitudes are boost invariant and may be discussed in any frame, it is convenient to imagine that we do not change the momentum of one of the hadrons, and that all the energy increase is achieved by boosting the second hadron. This is illustrated in Fig. 7. The gray/blue strip, unchanged compared to the low energy case, may be viewed as the size of the first hadron, that we did not boost. All the changes are in the internal dynamics of the second hadron, whose timescales are now stretched by Lorentz time dilation. The gluon exchanges between the valence quarks are now happening over timescales that are much longer than the duration of the collision, which means that the constituents of the nucleon can be viewed as free during the collision. The same happens to all the fluctuations of the constituents. The lifetime of these virtual states is increased much beyond the collision timescales, making these off-shell constituents undistinguishable from on-shell particles[4]. Since there are fluctuations at arbitrary small timescales in a nucleon at rest, increasing the energy will uncover more and more of these fluctuations. These simple kinematical considerations are the essence of the *parton model*, that approximates a high energy nucleon or nucleus as a collection of quasi-free constituents (called partons), and whose distributions grows with energy.

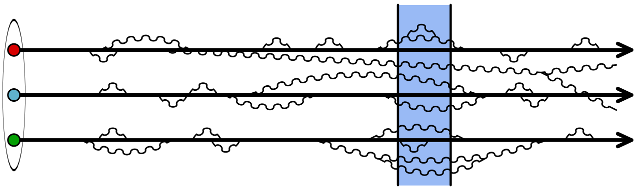

Fig. 7. Dynamics of the constituents inside a highly boosted nucleon.

2.2. Factorization

From this discussion, it seems that a QCD description of high energy collisions between hadrons may be feasible, provided we can provide "snapshots" of their partonic content at the time of the collision. What information is

---

[4] The concept of on-shell or off-shell particles depends on the duration of the measurement. The only way to know that a particle is really on-shell is to perform an infinitely long measurement. Indeed, an off-shell particle may be viewed as a particle of momentum $\boldsymbol{p}$ whose energy differs from the on-shell energy $E_{\boldsymbol{p}}$ given by the dispersion relation. A measurement that lasts Δt can only resolve energy differences of the order of $1/\Delta t$ or larger.

necessary in this snapshot is not completely obvious at this point, and may vary depending on the observable one intends to calculate, but, for instance, one may think of the following:

— flavor and color of each parton,

— transverse position and longitudinal momentum.

Of course, these properties of a hadron cannot be known event-by-event, which means that at best a probabilistic description may be achieved, that would allow to compute expectation values for event averaged observables. The possibility of describing hadronic collisions with only a probabilistic partonic description of the incoming hadrons is highly non-trivial, because it is an approximation that amounts to discarding certain quantum interferences. Without doing any approximation, the transition probability from a pair of hadrons h_1h_2 to some final state is obtained by summing all the reaction channels to the *amplitude* before squaring the amplitude,

$$\begin{matrix}\text{transition probability}\\ \text{from hadrons to } X\end{matrix} \equiv \left|\sum \begin{matrix}\text{Amplitudes}\\ h_1h_2 \to X\end{matrix}\right|^2 .$$

In contrast, the parton model described above would express the transition probability as follows,

$$\begin{matrix}\text{transition probability}\\ \text{from hadrons to } X\end{matrix} \equiv \sum_{\substack{\text{partons}\\ \{q,g\}}} \begin{matrix}\text{probability to find}\\ \{q,g\} \text{ in } \{h_1,h_2\}\end{matrix} \otimes \left|\sum \begin{matrix}\text{Amplitudes}\\ \{q,g\} \to X\end{matrix}\right|^2$$

which is clearly an approximation of the previous formula. This approximation is called *initial state factorization.* Roughly speaking, the physical motivation for such a factorization is that the neglected terms are interferences between a hard process that occurs on the timescale of the collision and a process internal to one of the projectiles, happening on much longer timescales. The vast separation in their timescales is what makes the corresponding interference small. At a more formal level, this factorization can be established in QCD, with various degrees of sophistication[5] depending on the observable.

---

[5] The weakest of these *factorization theorems* are *leading log factorization*, where the two formulas are shown to be equivalent for an infinite series of terms of the form $(\alpha_s \log(Q))^n$ (where Q is some hard scale) but perhaps not for terms of the form $\alpha_s(\alpha_s \log(Q))^n$. *Next-to-leading log factorization* extends the proof of this equivalence to include terms in $\alpha_s(\alpha_s \log(Q))^n$, and so on. *All-orders factorization theorems* prove that the two formulas are equivalent up to terms that decrease as inverse powers of the hard scale.

2.3. Single parton distributions

The most developed framework for this kind of factorization is the DGLAP formalism, in which one describes the incoming hadrons by *single parton distributions.* These distributions depend on the hadron and on the parton under consideration, on the fraction x of longitudinal momentum carried by the parton, and on a momentum scale Q that can be viewed as the inverse of the transverse spatial resolution with which the hadron is probed.

In Fig. 8, the single parton distributions of a proton, extracted from deep inelastic scattering data, are shown at a fixed resolution scale Q. Although these distributions are non-perturbative and cannot be computed from the QCD Lagrangian, QCD predicts how they change if one increases the resolution scale Q, via the *DGLAP equation* [2–5]. From this figure, one sees that the valence quark distribution is predominant at large values of the momentum fraction $x \gtrsim 0.1$, and is totally negligible at small x. At any value $x \lesssim 0.1$, the gluons are the dominant species of partons, and their density increases like a power of $1/x$ when $x \to 0$. The sea quarks follow the trend set by the gluons, but with a suppression factor of the order of $\alpha_{\rm s}$ since they are produced by the process $g \to q\bar{q}$.

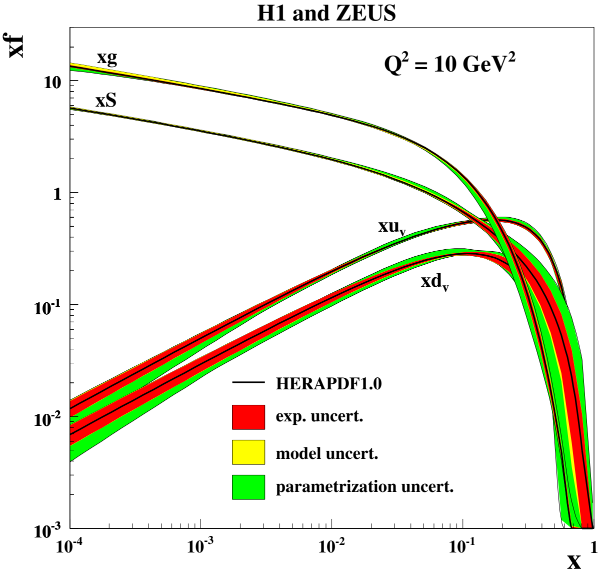

Fig. 8. Parton distributions of a proton at the resolution scale $Q^2 = 10$ GeV^2. From [1].

3. Gluon saturation

3.1. Dense regime of QCD

Since the DGLAP factorization framework is based solely on the single parton distributions, it is expected to become inappropriate at large parton densities. The problem that will arise in this regime is illustrated in Fig. 9, that shows side-to-side a typical scattering process in the dilute (left) and dense (right) regimes. In the dilute situation, the incoming hadrons are "mostly empty", and hard scatterings are rare processes. Moreover, reactions involving more than one parton in each projectile are extremely rare (their rate scales like the square of the probability to find a parton). But when the parton density is large, processes initiated by multiple partons become more likely to happen. A framework that would enable one to calculate these processes should provide information about multiparton distributions in hadrons and nuclei, and thus should go beyond the DGLAP framework. Moreover, when the parton density becomes of the order of the inverse coupling $1/g^2$, a strongly interacting regime, called *gluon saturation* [6–8], is reached, where an infinite series of Feynman graphs contribute at each order in g^2.

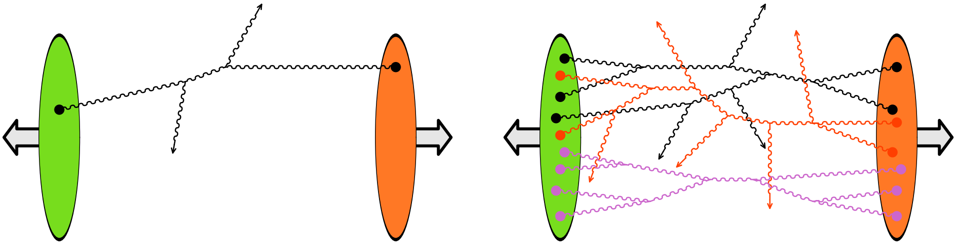

Fig. 9. Differences between a collision between dilute and dense projectiles.

A hint of the fact that the small x saturation regime is qualitatively different from the dilute regime appears when plotting the deep inelastic scattering cross section slightly differently. This cross section depends on two Lorentz invariant quantities, x and the 4-momentum squared Q^2 of the photon exchanged in the scattering. However, when plotted against the combination $x^{0.32}Q^2$, this data appears to line up on a unique curve (see Fig. 10). This scaling indicates the emergence of an x-dependent momentum scale, that behaves roughly as $Q_{\rm s}^2(x) \sim x^{-0.32}$. This scale, known as the *saturation momentum*, appears as a consequence of the non-linear interactions among the gluons, that become important at high density.

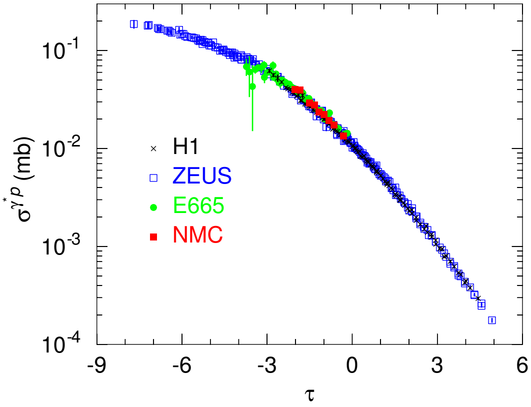

Fig. 10. Geometrical scaling in the DIS cross section at small x.

3.2. Saturation condition

To understand the onset of gluon saturation, it is instructive to go back to the dilute regime at large x. In this situation, a hadron appears as a loose collection of a few partons. When the hadron is progressively boosted, these partons radiate more gluons by bremsstrahlung[6], as illustrated in the top panel of Fig. 11. As long as the density remains low enough, these cascades of gluons develop independently and the evolution[7] of the hadron structure is governed by the linear *BFKL equation* [9, 10]. Since these additional gluons are contained within the geometrical volume of the hadron, their density increases rapidly. At some point, their wavefunctions start to overlap and their interactions are no longer negligible. Gluons from two different cascades can recombine, which tames the growth of the gluon density. Moreover, this recombination process makes the x evolution of the gluon distribution non-linear.

Before going into a more quantitative description of gluon saturation, it is easy to derive a simple criterion for the onset of saturation. Roughly speaking, gluon recombination becomes likely if the product of the numbers of gluons per unit area with the cross section for recombining two gluons into one becomes larger than one

$$\underbrace{\alpha_{\rm s} Q^{-2}}_{\sigma_{gg\to g}} \times \underbrace{A^{-2/3} xG\left(x,Q^2\right)}_{\text{surface density}} \geq 1\,. \tag{4}$$

---

[6] As discussed before, these gluons are not truly on-shell, but can be viewed as real gluons if the lifetime of the quantum fluctuation that gave them birth is longer than the observation time.

[7] Although this terminology is commonly used, it is a misnomer, since the hadron does not truly “evolve”. It is the observer’s view of the hadron content that changes as the observer’s frame is increasingly boosted with respect to the hadron.

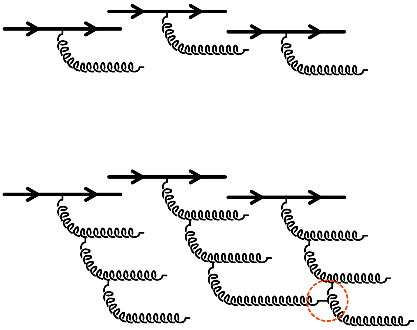

Fig. 11. Gluon cascades in the small x evolution of a hadron. Top: dilute regime. Bottom: onset of the recombination corrections.

This condition can be massaged to obtain an inequality on Q

$$Q^2 \le \underbrace{Q_\mathrm{s}^2 \equiv \frac{\alpha_\mathrm{s} xG\left(x, Q_\mathrm{s}^2\right)}{A^{2/3}}}_{\text{saturation momentum}} \sim A^{1/3} x^{-0.3} \,. \tag{5}$$

This argument justifies the emergence of the saturation momentum, which characterizes the physics of gluon saturation. Saturation is important when the typical momentum scales in a process are below Q_s. The region where this condition is satisfied is shown in Fig. 12. From the more quantitative plot on the right-hand panel of this figure, a typical value to keep in mind is that Q_s^2 is in the range of 2–4 GeV^2 for nuclei at the energy of the LHC. In the saturation domain, non-linear gluon interactions are important, which arguably makes the calculation of such processes more complicated. However, this also has an unexpected positive aspect: Q_s now supersedes all the

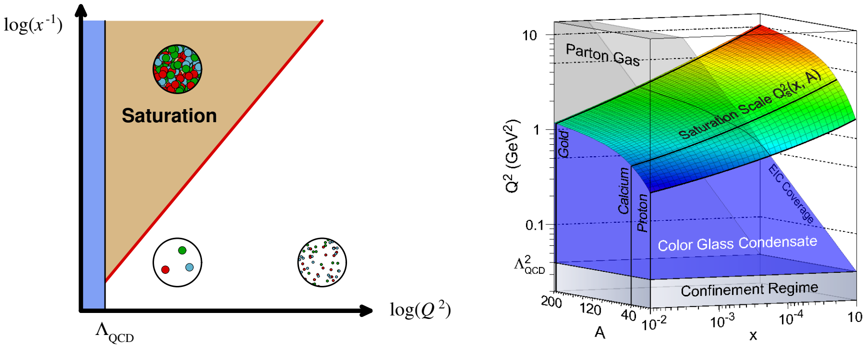

Fig. 12. Saturation domain in the x and Q plane. The 3-dimensional plot on the right-hand side adds information about the A dependence. From [11].

softer momentum scales in determining the typical momentum of the relevant partons, and thus also controls the running of the coupling. Since Q_s increases when x decreases (*i.e.* when going at higher energy), this opens an avenue for an *ab initio* perturbative treatment of multiparton interactions (sometimes called the "underlying event" in other contexts) in high energy hadronic scatterings. From Eq. (5), one sees that the saturation momentum also increases with the mass number of nuclei. This implies that, at a given energy, saturation effects are stronger in nucleus–nucleus collisions, for large nuclei[8]. This is important for heavy ion collisions at the RHIC and the LHC, because in these collisions the bulk of particle production is controlled by saturation physics.

4. Color Glass Condensate

4.1. Degrees of freedom

The Color Glass Condensate[9] (CGC) is a QCD-based effective theory whose aim is to describe quantitatively the gluon saturation regime. The CGC uses the high energy kinematics in order to simplify the description of the non-perturbative valence partons. The main idea was already encountered in the qualitative discussion of the parton model: a high energy hadronic collision is so brief that the fact that the partons are strongly bound by confinement is totally irrelevant. In fact, over such short timescales, the internal motion of the partons inside the hadron appears completely frozen. Thus, one may view the partons as static in the transverse plane, with a large longitudinal momentum [16–18]. For an observer sitting in the center-of-mass frame of the collision, the only information that matters about these partons is the color current J_a^μ they carry. The dominant component of this 4-vector is the longitudinal one. In light-cone coordinates, for a hadron moving in the $+z$ direction, this reads

$$J_a^\mu(x) = \rho_a(x^-, \boldsymbol{x}_\perp)\, \delta^{\mu +} \,. \tag{6}$$

The function $\rho_a(x)$ is the density of color charges of the partons. It does not depend on the light-cone "time" x^+ because of time dilation. Moreover, due to Lorentz contraction, its x^- dependence is very peaked around $x^- = 0$.

It is important to realize that this drastic simplification cannot be used for all partons: it is applicable only to those partons whose longitudinal momentum (in the observer's frame) is large enough. The partons that have a rapidity close to the observer's rapidity have comparable transverse and

---

[8] For gold or lead nuclei, the factor $A^{1/3}$ that appears in Q_s^2 is approximately 6.

[9] For more detailed reviews of the Color Glass Condensate, one can consult Refs. [12–15].

longitudinal momenta, and thus cannot be approximated by a longitudinal current. Moreover, for these partons, the Lorentz boost factor that slows down their time evolution is not very important and one cannot neglect their dynamics. Therefore, these slower partons must be treated as full fledged quantum fields. The situation is summarized in Fig. 13: a cutoff must be introduced between the rapidity of the observer and the rapidity of the hadron under consideration. The partons close to the observer (mostly gluons) are described as gauge fields, while those that are close to the projectile are approximated as a color current.

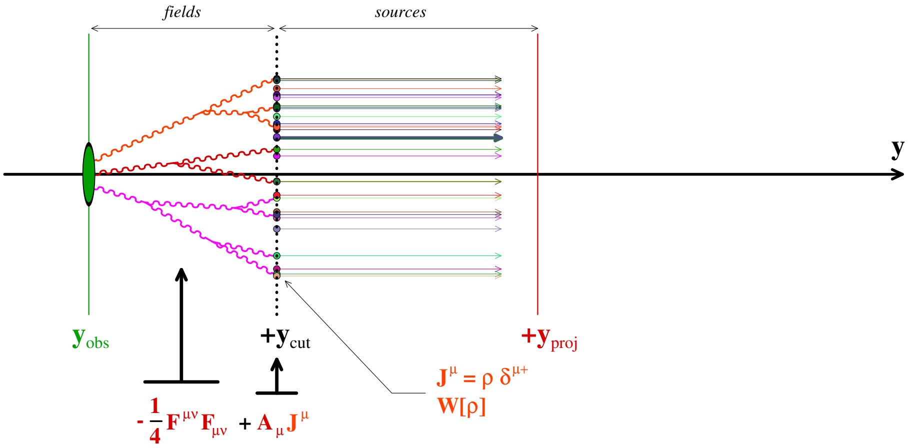

Fig. 13. Degrees of freedom in the CGC effective theory.

4.2. CGC effective theory

Thanks to the rapidity separation between the slow and the fast degrees of freedom in the CGC, their coupling can be treated as eikonal, *i.e.* via a term of the form $J^\mu A_\mu$. Therefore, the CGC can be summarized by the following effective action

$$\mathcal{S}_{\rm CGC} = \int d^4x\ \left(-\tfrac{1}{4}F_{\mu\nu}F^{\mu\nu} + J^\mu A_\mu\right)\ . \tag{7}$$

(For a collision of two hadrons, the current J^μ is the sum of two terms, one for each hadron.) The function $\rho_a(x^-, \boldsymbol{x}_\perp)$ that appears in the current J^μ reflects the particular arrangement of the fast partons at the time of the collision. It is not a quantity that can be predicted event-by-event, and one can only have a statistical knowledge of this object. Therefore, the CGC introduces a probability distribution $W[\rho]$. As we shall see later, all observable quantities must be averaged over all the possible configurations of ρ, according to the distribution $W[\rho]$

$$\langle \mathcal{O} \rangle = \int [D\rho]\; W[\rho]\, \mathcal{O}[\rho]\,. \tag{8}$$

In other words, one should first calculate the observable for an arbitrary configuration of the color charge density ρ (in a collision of two hadrons, there is a ρ_1 and a ρ_2), and then perform a weighted average over all the possible ρs. The justification of this procedure will be given in the following two sections.

5. CGC at leading order

5.1. Power counting

So far, we have not made any assumption about the magnitude of the color charge density ρ_a that describes the fast partons in the CGC effective theory. For the CGC to be applicable to the saturated regime, we must allow ρ_a to be as large as the inverse coupling $1/g$. Indeed, the recombinations due to non-linear gluon interactions can stabilize the gluon occupation number at a value of the order of $1/g^2$. Since the occupation number is quadratic in the gauge field, such a value corresponds to $\rho \sim g^{-1}$. As we shall see, such a large value of the source ρ simplifies the dynamics by making it classical at leading order, but complicates things by making an infinite set of graphs contribute at each order in g^2. In order to see this, let us first examine the power counting in the CGC effective theory. Consider a generic connected graph, as shown in Fig. 14. For such a graph, one finds that the order of magnitude depends only on the number of produced gluons and the number

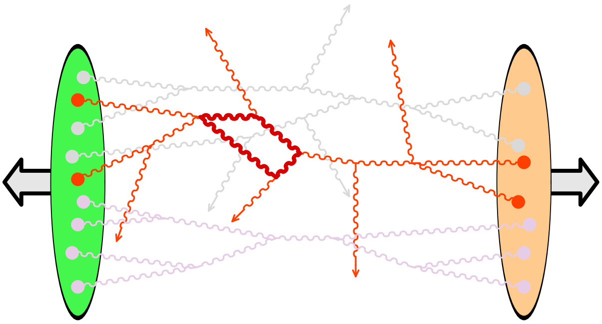

Fig. 14. Generic connected graph in the CGC effective theory. The dots represent the sources ρ.

of loops, via the following formula [19, 20]

$$\frac{1}{g^2}\; g^{\#\text{ produced gluons}}\; g^{2(\#\text{ loops})}\,. \tag{9}$$

The main consequence of assuming that $\rho \sim g^{-1}$ is that this power counting does not depend on the number of sources that are inserted into the graph. The reason for this is that each additional source (of the order of g^{-1}) is attached to the rest of the graph by a vertex (of the order of g), and therefore does not contribute to the overall magnitude of the graph. This also means that, at each order in g^2, one must sum an infinite set of graphs.

For instance, the inclusive gluon spectrum has the following expansion in powers of g^2

$$\frac{dN_1}{d^3\vec{\boldsymbol{p}}} = \frac{1}{g^2}\left[c_0 + c_1\,g^2 + c_2\,g^4 + \dots\right], \tag{10}$$

where each of the coefficients $c_0, c_1, \dots$ is itself an infinite series of terms of the form $(g\rho)^n$

$$c_i \equiv \sum_{n=0}^{\infty} c_{i,n}\,(g\rho_{1,2})^n\,. \tag{11}$$

At this point, we should make an important remark regarding exclusive *versus* inclusive observables. From the above power counting, we see that the average number of produced gluons in a high energy nucleus–nucleus collisions is of the order of $1/g^2$. If we assume for simplicity that the multiplicity distribution is Poissonian[10], the probability to have a given final state (*i.e.* a final state with a prescribed number of gluons) is exponentially suppressed by a factor $\exp(-\#/g^2)$. This factor may be viewed as the Sudakov factor that arises when excluding all the other final states. It turns out that these exclusive quantities are very difficult to calculate. In contrast, many simplifications occur in the calculation of inclusive quantities, that involve an average over all possible final states

$$\big\langle\mathcal{O}\big\rangle \equiv \sum_{\substack{\text{all final}\\ \text{states }\boldsymbol{f}}} \mathcal{P}(AA\to\boldsymbol{f})\;\mathcal{O}[\boldsymbol{f}]\,. \tag{12}$$

In particular, the high energy factorization results that will be discussed in the next section can only be established for these inclusive quantities, and their proof fails if one tries to generalize it to exclusive quantities.

---

[10] This is not exactly true in the CGC, but this fact does not change the essence of this argument.

5.2. Calculation of inclusive observables

The definition of Eq. (12) suggests a possible method for calculating an inclusive quantity: compute the exclusive probabilities to end up in a given final state f, and sum over all possible fs. However, it turns out that one can calculate them in a much more effective way without having to perform explicitly the sum over the final states. For this, one should use the *Schwinger–Keldysh formalism* [21, 22], in which this sum is already "built in". Any contribution to Eq. (12) is the product of an amplitude, a complex conjugate amplitude going to the same final state, and the observable evaluated on this final state, as illustrated in Fig. 15. The diagrammatic rules for the amplitude (right of the vertical line) are the usual time-ordered Feynman rules. The propagator is the usual Feynman propagator, which for a scalar particle reads

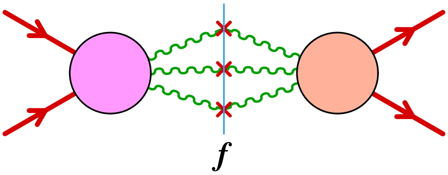

Fig. 15. Illustration of the Schwinger–Keldysh formalism.

$$G^0_{++}(p) = \frac{i}{p^2 + i\epsilon}\,. \tag{13}$$

For the complex conjugate amplitude (left of the vertical line), one needs the complex conjugate of the vertices and propagators. The propagator is

$$G^0_{--}(p) = \frac{-i}{p^2 - i\epsilon}\,. \tag{14}$$

Across the vertical line, one must use special propagators that represent the on-shell particles of the final state f

$$G^0_{+-}(p) = 2\pi\theta\left(-p^0\right)\delta\left(p^2\right)\,. \tag{15}$$

The Schwinger–Keldysh formalism amounts to the following:

- Draw all the graphs $AA \to AA$ that have a given order in g^2 (the power counting is the same as before, with each loop adding one power of g^2).
- Sum over all the possibilities of assigning the labels $+$ and $-$ to the internal vertices.
- Only connected graphs contribute. When summed over the $+$ and $-$ labels, the disconnected graphs that are not attached to the observable cancel.

These rules will automatically provide the sum over final states that was included in the formula (12). Note that when used in this context, the Schwinger–Keldysh formalism is equivalent to Cutkosky's cutting rules [23, 24], that were developed as a tool to compute the imaginary part of transition amplitudes. The superficial description of the Schwinger–Keldysh formalism that we have given here can be made more rigorous by writing the generating functional for its Green's functions. It can be obtained as follows from the generating functional $Z[j]$ of time-ordered perturbation theory

$$Z[j_+,j_-] = \exp\left[\int d^4x d^4y\, G^0_{+-}(x,y)\,\square_x\square_y\,\frac{\delta^2}{\delta j_+(x)\delta j_-(y)}\right] Z[j_+]\,Z^*[j_-]\,. \tag{16}$$

This formula makes more obvious the fact that the Schwinger–Keldysh formalism is made of two copies of the ordinary Feynman perturbation theory (one of them complex conjugated), "stitched" together by the on-shell propagators G^0_{+-}.

At this point, we have not really simplified the calculation of Eq. (12). It has just been rephrased in a more systematic language. The simplifications come from noticing the following identities

$$\begin{aligned} &G_{++}+G_{--}=G_{+-}+G_{-+}\,,\\ &G_{++}-G_{+-}=G_{-+}-G_{--}=G_{\rm R}\quad\text{(retarded propagator)}\,. \end{aligned}\tag{17}$$

When using the Schwinger–Keldysh formalism to calculate inclusive observables at leading order, the sum over the + and − indices always generates the particular combinations of propagators that appear in the second of these equations, and these propagators therefore become retarded propagators.

5.3. *Classical equation of motion*

This simplification is particularly dramatic for inclusive observables at leading order. The starting point is a double sum over all possible tree diagrams (they all have the same order in g^2 when the source is $\rho \sim g^{-1}$) and over all the indices + and − of the Schwinger–Keldysh formalism. Thanks to the previous remark, the second sum merely replaces all the propagators by retarded propagators. One is thus left with a sum over all the tree diagrams built with retarded propagators, whose first few terms would be

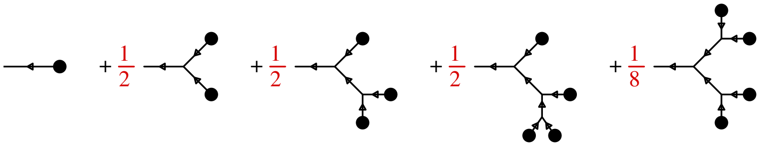

(here for a ϕ^3 scalar field theory.) It is then easy to see that this sum is the solution of the classical field equations of motion that vanishes when $x^0 \to -\infty$ (this retarded boundary condition follows from the fact that we are summing tree that are made of retarded propagators[11]). Although in interacting theories the classical equation of motion is a non-linear wave equation, this is a considerable simplification because we have now a problem that can be solved numerically.

The same simplifications work in the case of the CGC: at leading order, it is sufficient to solve the classical Yang–Mills equations with null retarded boundary conditions

$$\big[D_\mu, F^{\mu\nu}\big] = \rho_1\,\delta^{\nu +} + \rho_2\,\delta^{\nu -}\,, \qquad \lim_{x^0\to-\infty} A^\mu(x) = 0\,. \tag{18}$$

Assuming that we have solved this equation, all the inclusive observables at leading order can be expressed in terms of its solution. For instance, the single inclusive gluon spectrum is given by

$$\left.\frac{dN_1}{dY\,d^2\vec{\boldsymbol{p}}_\perp}\right|_{\text{LO}} = \frac{1}{16\pi^3}\int\limits_{x,y} e^{ip\,(x-y)}\,\square_x\square_y\,\sum_\lambda \epsilon_\lambda^\mu\epsilon_\lambda^\nu\;\mathcal{A}_\mu(x)\mathcal{A}_\nu(y)\,, \tag{19}$$

and inclusive multigluon spectra read

$$\left.\frac{dN_n}{d^3\boldsymbol{p}_1\cdots d^3\boldsymbol{p}_n}\right|_{\text{LO}} = \left.\frac{dN_1}{d^3\boldsymbol{p}_1}\right|_{\text{LO}} \times\cdots\times \left.\frac{dN_1}{d^3\boldsymbol{p}_n}\right|_{\text{LO}}\,. \tag{20}$$

Similarly, the components of the energy-momentum tensor have simple expressions in terms of the classical chromo-electric and chromo-magnetic fields $\boldsymbol{E}^i$ and $\boldsymbol{B}^i$

$$T^{00}_{\text{LO}} = \frac{1}{2}\left[\boldsymbol{E}^2 + \boldsymbol{B}^2\right]\,, \qquad T^{0i}_{\text{LO}} = \left[\boldsymbol{E}\times\boldsymbol{B}\right]^i\,, \tag{21}$$

$$T^{ij}_{\text{LO}} = \frac{\delta^{ij}}{2}\left[\boldsymbol{E}^2 + \boldsymbol{B}^2\right] - \left[\boldsymbol{E}^i\boldsymbol{E}^j + \boldsymbol{B}^i\boldsymbol{B}^j\right]\,. \tag{22}$$

---

[11] One can see here why it is important to consider inclusive observables for this simplification to happen. It is the sum over the final states that leads to the sum over the indices + and −. Without this sum, one would be left with time-ordered propagators, which would make the boundary conditions of the classical solution untractable.

5.4. Numerical implementation

In order to perform this calculation in practice, we have to be aware of the following:

- *(i)* High energy collisions are nearly invariant under boosts in the longitudinal direction. This invariance has its simplest manifestation if one uses proper-time ($\tau \equiv \sqrt{2x^+x^-}$) and rapidity ($\eta \equiv \frac{1}{2}\log(x^+/x^-)$) as the coordinates inside the forward light-cone. When written in this system of coordinates, the classical Yang–Mills equations do not depend on rapidity, and thus become 1+2 dimensional equations.
- *(ii)* The sources ρ_1 and ρ_2 have support on the light-cone, where they are singular, *i.e.* proportional respectively to $\delta(x^-)$ and $\delta(x^+)$. These sources divide the space time in four distinct regions, as shown in the left-hand side of Fig. 16. The gauge field is identically zero in the region 0, and it can be found analytically in the regions 1 and 2 [25]. In the region 3, the best one can do analytically is to obtain the value of the gauge fields just above the forward light-cone, at a proper time $\tau = 0^+$ [26].

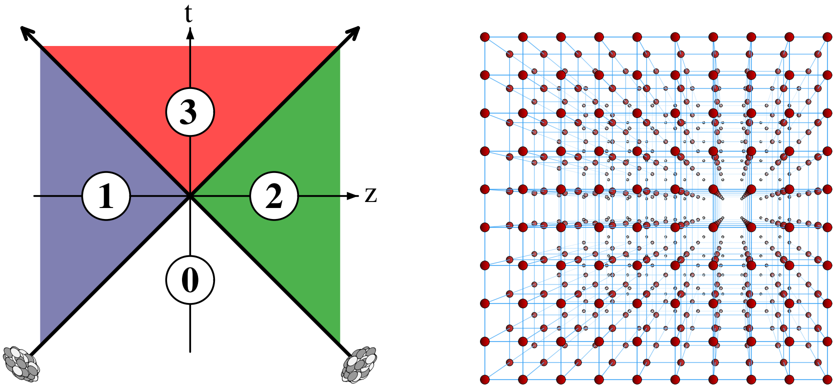

Fig. 16. Left: space-time structure of the classical gauge field. Right: 3-dimensional cubic lattice.

Given these remarks, we need only to solve numerically the Yang–Mills equations in the forward light-cone [27–36]. Choosing the time variable τ determines the Hamiltonian of the system, and from there one can determine the Yang–Mills equations in Hamiltonian form. In order to handle them numerically, one must discretize space on a cubic lattice (see the right-hand side of Fig. 16), while time remains a continuously varying variable. This is best done in the temporal gauge $A^\tau = 0$ (also called the Fock–Schwinger gauge in this context). After having adopted this gauge condition, the problem has a residual gauge invariance, under any gauge transformation that depends only on space. Naive discretizations based on the gauge potentials A^μ are inappropriate because they lead to violations of this residual gauge invariance. Instead, one should adopt Wilson's formulation, in which the gauge potentials are traded in favor of link variables (see the left-hand side of Fig. 17), *i.e.* Wilson lines that span one elementary edge of the lattice

$$U_i(x) \equiv \mathrm{P}\,\exp i\,g \int\limits_{x}^{x+\hat{\imath}} ds\; A^i(s)\,. \tag{23}$$

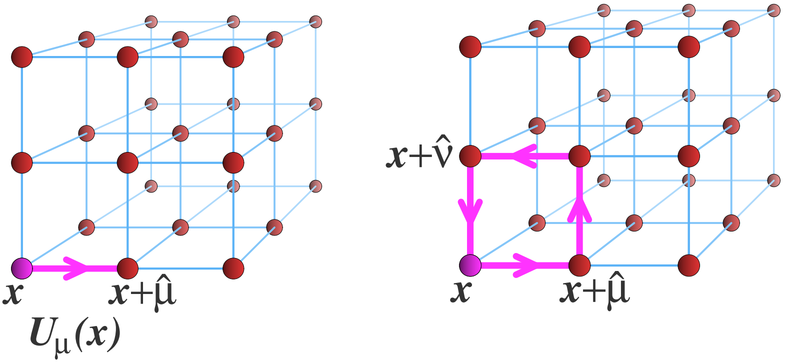

Fig. 17. Left: link variable. Right: elementary plaquette variable.

Under a residual gauge transformation, these links transform as

$$U_i(x) \quad\to\quad \Omega(x)\,U_i(x)\,\Omega^\dagger\,(x+\hat{\imath})\,. \tag{24}$$

The electrical fields E_i that appear in Hamilton's equations transform covariantly,

$$E_i(x) \quad\to\quad \Omega(x)\,E_i(x)\,\Omega^\dagger(x)\,, \tag{25}$$

and therefore they should live on the nodes of the lattice. In the $A^\tau = 0$ gauge, the Hamiltonian discretized in this fashion reads

$$\begin{aligned}\mathcal{H} &= \sum_{\vec{\boldsymbol{x}};i} \frac{E^i(\boldsymbol{x})E^i(\boldsymbol{x})}{2}\\ &\quad -\frac{6}{g^2}\sum_{\vec{\boldsymbol{x}};ij} 1-\frac{1}{3}\mathrm{Re}\ \mathrm{Tr}\,(\ \underbrace{U_i(x)U_j(x+\hat{\imath})U_i^\dagger(x+\hat{\jmath})U_j^\dagger(x)}_{\text{plaquette at the point } \tilde{\boldsymbol{x}} \text{ in the } ij \text{ plane}}\ )\,.\end{aligned} \tag{26}$$

The only combinations of link variables that enter in this formula are *plaquettes* (*i.e.* the trace of the product of the four link variables that form an elementary square on the cubic lattice), which are gauge invariant. The Hamilton equations that can be derived from this Hamiltonian form a large (but finite) set of ordinary differential equations, that can be solved numerically by standard methods such as the leapfrog algorithm.

5.5. Structure of the classical color fields

At very short times after the collisions ($\tau \ll Q_s^{-1}$), the classical chromo-electric and chromo-magnetic fields are parallel to the collision axis [37], as illustrated in Fig. 18. By studying how the expectation value of Wilson loops,

$$W \equiv \left\langle \mathrm{P}\,\exp ig \int_\gamma dx^i \mathcal{A}^i \right\rangle , \tag{27}$$

depends on the area enclosed by the loop, one can infer the typical transverse size of these flux tubes. Indeed, one can roughly view the argument of the exponential as the magnetic flux going through the loop. It has been found that W decreases roughly as $\exp(-\# \times \text{Area})$ for areas larger than Q_s^{-2}, which indicates that the fields are not correlated over transverse distances larger than Q_s^{-1}. Q_s^{-1} is, therefore, the typical radius of these flux tubes.

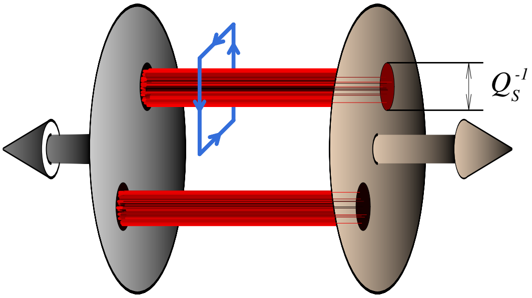

Fig. 18. Color flux tubes just after the collision.

From the classical gauge fields, one can compute the spectrum of gluons produced in a heavy ion collision (see Fig. 19). At large transverse momentum, the spectrum decreases as $k_\perp^{-4}$. Indeed, when $k_\perp \gg Q_s$, the saturation criterion is not satisfied and one should recover the usual perturbative results of the dilute regime. In contrast, saturation effects are quite large at small transverse momentum, $k_\perp \lesssim Q_s$, where they produce a strong softening of the spectrum, while the dilute result would still give a spectrum that grows as $k_\perp^{-4}$ at small $k_\perp$ (because there is no dimensionful scale other than $k_\perp$

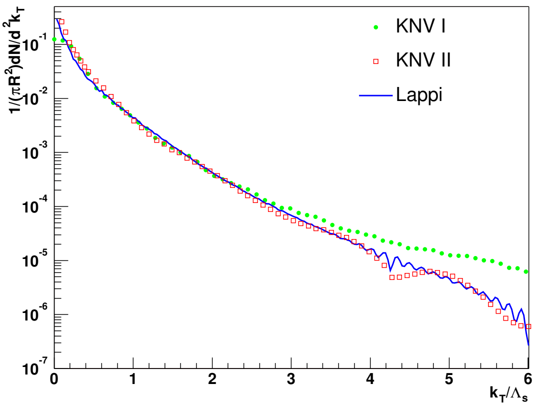

Fig. 19. Inclusive gluon spectrum.

in the dilute calculation). Let us close this section by a remark concerning the energy dependence of the gluon multiplicity, obtained by integrating the gluon spectrum over $k_\perp$. The result is proportional to the transverse area times Q_s^2,

$$N_{\rm gluon} \sim \frac{S_\perp Q_{\rm s}^2}{\alpha_{\rm s}}\,. \tag{28}$$

From this pocket formula, one sees that the energy dependence of the gluon multiplicity is directly inherited from that of the saturation momentum,

$$N_{\rm gluon} \sim x^{-0.3} \sim s^{0.15}\,. \tag{29}$$

Note that there is no contradiction between the fact that the multiplicity grows like a power of the collision energy and the Froissart bound, that tells us that hadronic cross sections cannot grow faster than $\sigma \sim \log^2(s)$. The difference between the two is due to the fact that these two objects measure two different things. The total cross section measures the probability that the two projectiles interact. As a probability, its growth is constrained by unitarity. In contrast, the gluon multiplicity measures the "amount of stuff" which is produced in a collision. It is not a probability, and is not bound by the same constraints. More precisely, the Froissart bound is related to the growth of the radius of the "black disk" region with energy (this radius grows like the log of energy). However, even after a certain region has become "black" (and thus its probability of interacting cannot grow anymore, because it has reached the unitarity limit), the number of gluons produced in this region will continue to grow like a power of energy (because the number of gluons per unit area in the incoming projectile scales like Q_s^2).

6. Next to leading order

6.1. Improved power counting

From the power counting formula derived earlier, we expected for the gluon spectrum an expansion of the form

$$\frac{dN}{d^3\vec{\boldsymbol{p}}} = \frac{1}{g^2}\left[c_0 + c_1\,g^2 + c_2\,g^4 + \dots\right], \tag{30}$$

and we have seen in the previous section how to calculate the term c_0/g^2. The following terms, $c_1, c_2 g^2, \dots$, are given respectively by the sum of 1-loop, 2-loop, *etc.* diagrams. When calculating loops in the CGC framework, we have to recall that the degrees of freedom have been divided into sources and fields, separated by a cutoff $y_{\rm cut}$ in rapidity. In the integration over the loop momentum, we must use this cutoff in order to prevent the loop momentum to go into the kinematical domain which is described in terms of static sources. Failing to do this would lead to a double counting of the contribution of the modes that lie in this region.

In general, loop diagrams will depend on this cutoff [38]: a graph with n loops can lead to up to n powers of $y_{\rm cut}$. Therefore, the coefficients that appear in the g^2 expansion of the gluon spectrum can themselves be expanded in powers of the cutoff as follows

$$\begin{array}{lcccccc} c_1 & = & & & c_{10} & + & c_{11}\,y_{\rm cut}\,, \\ c_2 & = & c_{20} & + & c_{21}\,y_{\rm cut} & + & \underbrace{c_{22}\,y_{\rm cut}^2}_{\text{leading log terms}}\,. \end{array} \tag{31}$$

The terms that have the maximal degree in $y_{\rm cut}$, *i.e.* a degree equal to the number of loops, are called *leading log terms*[12].

The cutoff $y_{\rm cut}$ was introduced by hand when defining the CGC, as a way of separating the two kinds of degrees of freedom, and it is therefore not a physical parameter. Observables should not depend upon it. As we shall see in this section, the leading log cutoff dependence that arises from loop corrections to observables can be absorbed into a redefinition of the probability distribution $W[\rho]$. This redefinition turns $W[\rho]$ into a cutoff dependent object, but its cutoff dependence is universal, which means that the same distributions can be used for all inclusive observables.

Before we continue with a discussion of the leading log terms, let us mention the fact the cutoff independent part of the NLO correction is now known in some cases: in the BK equation (a mean field approximation of

---

[12] The terminology comes from the fact that $y_{\rm cut}$ is the logarithm of a cutoff on the longitudinal momentum.

the JIMWLK equation) [39–42] and also for the JIMWLK equation [43–45]. The running coupling corrections have been used in phenomenological studies [46–50] where they appear to be quantitatively important.

6.2. NLO result and cutoff dependence

Let us give here a sketch of the proof of this statement. The first step is the derivation of an expression for the NLO correction to inclusive observables. It turns out that there exists a formal relationship between the LO and NLO contributions, valid for any inclusive observable, that reads [51, 52]

$$\mathcal{O}_{\rm NLO}=\left[\frac{1}{2}\int\limits_{\boldsymbol{u},\boldsymbol{v}}\boldsymbol{\Gamma}_2(\boldsymbol{u},\boldsymbol{v})\,\frac{\partial}{\partial\mathcal{A}_{\rm init}(\boldsymbol{u})}\frac{\partial}{\partial\mathcal{A}_{\rm init}(\boldsymbol{v})}+\int\limits_{\boldsymbol{u}}\boldsymbol{\alpha}(\boldsymbol{u})\,\frac{\partial}{\partial\mathcal{A}_{\rm init}(\boldsymbol{u})}\right]\mathcal{O}_{\rm LO}\,. \tag{32}$$

In this formula, the LO observable $\mathcal{O}_{\rm LO}$ should be viewed as a functional of the initial value (generically denoted $\mathcal{A}_{\rm init}$ in the previous equation) on some space-like hypersurface (the integrations over the variables $\boldsymbol{u}$ and $\boldsymbol{v}$ are on this surface). The remarkable property here is that the coefficient functions $\boldsymbol{\Gamma}_2$ and $\boldsymbol{\alpha}$ are universal in the sense that they do not depend on the observable under consideration. However, although this formula is valid for all inclusive observables, it is not true for exclusive observables.

Note that in this formula, the operator between the square brackets acts only on the initial value of the classical fields, while the time evolution from the initial time surface to the time where the observable is evaluated remains classical. This is, in fact, a completely general result in quantum mechanics: at the first order in $\hbar$, the time evolution remains classical and $\hbar$ enters only in the initial condition. This is not true beyond NLO: at the second order in $\hbar$, the quantum effects start affecting the time evolution itself.

Equation (32) is very useful in order to extract the cutoff dependence in inclusive observables at NLO. In fact, this cutoff dependence is already present in the operator that acts on $\mathcal{O}_{\rm LO}$. If we keep only the terms that are linear in the cutoff, we have [51–53]

$$\frac{1}{2}\int\limits_{\boldsymbol{u},\boldsymbol{v}}\boldsymbol{\Gamma}_2(\boldsymbol{u},\boldsymbol{v})\,\frac{\partial}{\partial\mathcal{A}_{\rm init}(\boldsymbol{u})}\frac{\partial}{\partial\mathcal{A}_{\rm init}(\boldsymbol{v})}+\int\limits_{\boldsymbol{u}}\boldsymbol{\alpha}(\boldsymbol{u})\,\frac{\partial}{\partial\mathcal{A}_{\rm init}(\boldsymbol{u})}=y_{\rm cut}^{+}\,\mathcal{H}_1+y_{\rm cut}^{-}\,\mathcal{H}_2\,. \tag{33}$$

In this equation, $y_{\rm cut}^{+}$ and $y_{\rm cut}^{-}$ are the cutoffs corresponding to the right- and left-hand side, moving nucleus respectively, and $\mathcal{H}_{1,2}$ are operators known as the JIMWLK Hamiltonians[13] of the two nuclei [54–62],

---

[13] If one expands this Hamiltonian at small ρ, one can recover the BFKL equation [9, 10].

$$\mathcal{H} \equiv \frac{1}{2} \int_{\vec{\boldsymbol{x}}_\perp, \vec{\boldsymbol{y}}_\perp} \frac{\delta}{\delta \rho_a(\vec{\boldsymbol{x}}_\perp)} \chi_{ab}(\vec{\boldsymbol{x}}_\perp, \vec{\boldsymbol{y}}_\perp) \frac{\delta}{\delta \rho_b(\vec{\boldsymbol{y}}_\perp)} \,, \tag{34}$$

where

$$\begin{aligned} \chi_{ab}(\vec{\boldsymbol{x}}_\perp, \vec{\boldsymbol{y}}_\perp) \; &\equiv \; \frac{\alpha_{\rm s}}{4\pi^3} \int d^2\vec{\boldsymbol{z}}_\perp \frac{(\vec{\boldsymbol{x}}_\perp - \vec{\boldsymbol{z}}_\perp) \cdot (\vec{\boldsymbol{y}}_\perp - \vec{\boldsymbol{z}}_\perp)}{(\vec{\boldsymbol{x}}_\perp - \vec{\boldsymbol{z}}_\perp)^2 (\vec{\boldsymbol{y}}_\perp - \vec{\boldsymbol{z}}_\perp)^2} \\ &\times \Big[\Big(1 - \widetilde{U}^\dagger(\vec{\boldsymbol{x}}_\perp) \widetilde{U}(\vec{\boldsymbol{z}}_\perp)\Big) \Big(1 - \widetilde{U}^\dagger(\vec{\boldsymbol{z}}_\perp) \widetilde{U}(\vec{\boldsymbol{y}}_\perp)\Big) \Big]_{ab} \,. \end{aligned} \tag{35}$$

In this equation, $\widetilde{U}$ is a Wilson line in the adjoint representation, constructed from the gauge field A^+ such that $\boldsymbol{\nabla}_\perp^2 A^+ = -\rho$.

6.3. Factorization

The formula (33) leads to two important results:

(i) This formula is the *sum* of two terms corresponding to the two nuclei, but there is no cutoff dependent term mixing the two nuclei. This means that the cutoff dependent terms are intrinsic properties of the nuclei prior to their collision, and this is the reason why it is possible to eliminate them by redefining the distributions of the sources $\rho_{1,2}$ of the two projectiles.

(ii) Since the operator in the square brackets in Eq. (32) is the same for all inclusive observables, the cutoff dependence is equally universal. This is the reason why it will be possible to define cutoff dependent distributions $W[\rho_{1,2}]$ such that they cancel the cutoff dependence of all observables.

The property *(i)*, about the absence of mixing of the cutoff dependence between the two nuclei, can be understood simply in terms of causality. This is illustrated in Fig. 20. Indeed, the cutoff dependence arises from the phase-space integration of the soft gluons emitted by bremsstrahlung. Since they are soft, the formation time of these gluons is large: they cannot be emitted during the very brief duration of the collision, so they have to be emitted before the collision. Because the separation between the two nuclei is space-like until the collision, causality forbids any cutoff dependent term that would mix the two nuclei. The property *(ii)* also follows the same reasoning: gluon emissions that happen before the collision should be the same for all observables measured after the collision.

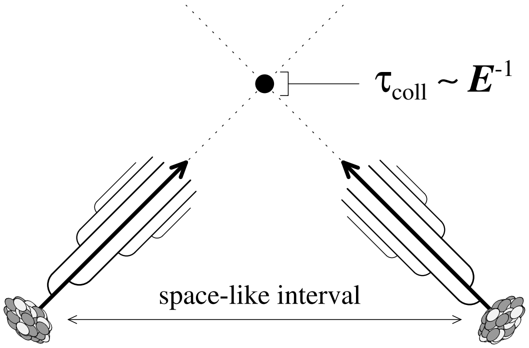

Fig. 20. Causality argument for factorization.

If we compute observables for fixed configurations ρ_1 and ρ_2 of the color charge densities in the two projectiles, there is no way to get rid of the cutoff dependence. The only way to remove it is to integrate over all possible $\rho_{1,2}$. The main ingredient in this manipulation is the fact that $\mathcal{H}$ is a self-adjoint operator

$$\int [D\rho]\, W\, (\mathcal{H}\,\mathcal{O}) = \int [D\rho]\, (\mathcal{H}\,W)\, \mathcal{O}\,. \tag{36}$$

This property can be used to transfer the action of $\mathcal{H}$ from the observable onto the distribution $W[\rho]$. From Eq. (33), one can see that ρ-averaged quantities such as

$$\frac{dN_1}{d^3\vec{\boldsymbol{p}}} \underset{\text{leading log}}{=} \int \left[D\rho_1\, D\rho_2\right] W_1\left[\rho_1\right]\, W_2\left[\rho_2\right]\, \underbrace{\left.\frac{dN_1}{d^3\vec{\boldsymbol{p}}}\right|_{\rm LO}}_{\text{fixed }\rho_{1,2}} \tag{37}$$

are independent of the cutoff, provided that the distributions $W[\rho]$ themselves depend on the cutoff according to the JIMWLK equation

$$\frac{\partial W}{\partial y} = \mathcal{H}\,W\,. \tag{38}$$

From Eqs. (32) and (33), it is furthermore obvious that the same factorization formula (with the same Ws) applies to any inclusive observable.

In Eq. (37), it is the evolution with rapidity of the distributions W that gives the gluon spectrum its rapidity dependence. Indeed, the gluon spectrum unintegrated over $\rho_{1,2}$ that enters in the integrands is independent of rapidity. From the JIMWLK equation, one sees that these distributions evolve significantly for changes of the rapidity of the order of $\Delta y \sim \alpha_s^{-1}$. This factorization result thus predicts that the spectrum should be rather flat in rapidity at weak coupling.

7. Ridge correlations

Equation (37) can be extended to the inclusive multigluon spectrum. Recalling also Eq. (20), we obtain the following factorization formula

$$\frac{dN_n}{d^3\vec{\boldsymbol{p}}_1\cdots d^3\vec{\boldsymbol{p}}_n} \underset{\text{leading log}}{=} \int \left[D\rho_1\, D\rho_2\right] W_1\left[\rho_1\right]\, W_2\left[\rho_2\right]\, \frac{dN_1}{d^3\vec{\boldsymbol{p}}_1}\cdots\frac{dN_1}{d^3\vec{\boldsymbol{p}}_n}\bigg|_{\text{LO}}\,. \tag{39}$$

This equation, valid at leading log accuracy, shows that at this order the correlations between the produced gluons only originate from correlations between the ρs of the incoming projectiles, since in the integrand the n gluons appear completely factorized. Since the relevant rapidity interval for a significant JIMWLK evolution is $\Delta y \sim \alpha_{\rm s}^{-1}$, this is also the typical rapidity distance over which the produced gluons will be correlated.

This is the basis of an interpretation of the peculiar shape of the 2-hadron correlations observed in heavy ion collisions. This correlation function is represented in Fig. 21, as a function of the relative azimuthal angle and relative rapidity. As one can see, the correlation is very narrow in azimuthal angle, and very elongated in rapidity[14]. Because of causality, the existence of a correlation between particles that are widely separated in rapidity must originate from phenomena that happened very shortly after the collision. This is explained in Fig. 22. Let us consider the time evolution of two particles A and B in reverse, starting from their last interaction on the freeze-out surface. Obviously, by causality, they must come from the light-cones represented respectively in dark grey/red and light grey/green in the figure. A correlation is an event that had an influence on both the particle A and the

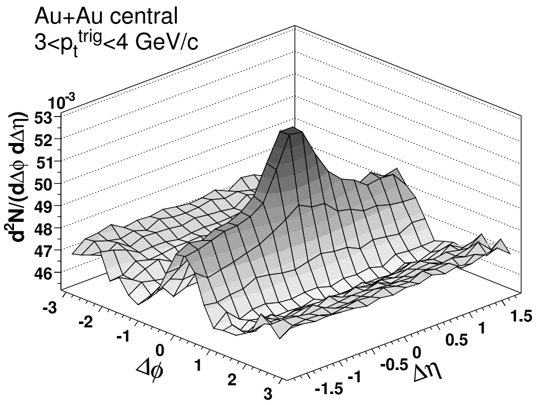

Fig. 21. Two hadron correlation measured in heavy ion collisions [63].

---

[14] The peak in the middle is a jet-like correlation, due to quasi-collinear splittings.

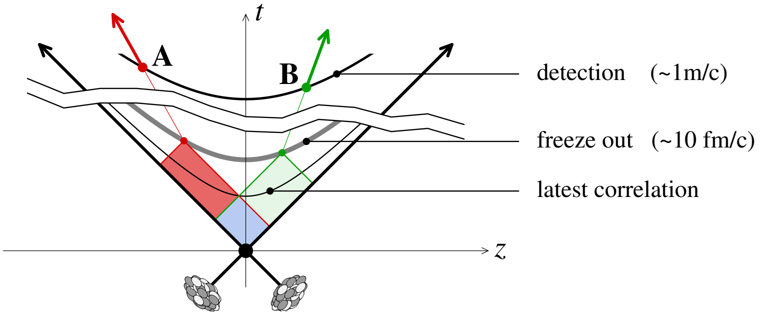

Fig. 22. Origin of the rapidity correlations.

particle B. It must, therefore, have happened in the overlap between these two light-cones, that we have represented in gray/blue. One sees clearly that there is a latest time at which this correlation could possibly have been created. From the time of the freeze-out and the rapidity separation of the two particles, it is easy to determine this upper bound of the time,

$$\tau_{\text{correlation}} \leq \tau_{\text{freeze out}}\ e^{-|\Delta y|/2}\,. \tag{40}$$

This bound decreases very rapidly as one increases the rapidity separation Δy. In heavy ion collisions, the order of magnitude of the freeze-out time is 10 fm/c. For instance, a correlation between particles separated in rapidity by $\Delta y = 6$ must be produced before the time 0.5 fm/c, which is well within the regime where the CGC is still applicable.

It is, in fact, easy to understand qualitatively the main features of the observed correlation from the structure of the classical color fields produced at early times in heavy ion collisions [64, 65]. As we have said before, they are organized in flux tubes that have a typical transverse size of Q_s^{-1} and that remain coherent over rapidity intervals of the order of α_s^{-1}. Two gluons emitted from the same tube are correlated if they are produced with a rapidity separation $\Delta y \lesssim \alpha_s^{-1}$, but are not correlated if they come from

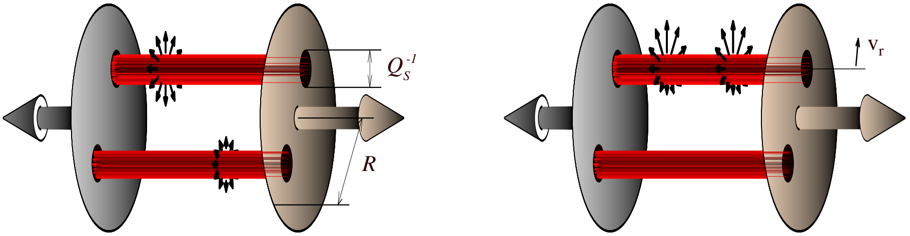

Fig. 23. Rapidity correlations from color flux tubes.

two different flux tubes[15] (see Fig. 23, left). From the size of the flux tubes, we conclude that the probability that two particles are correlated scales as $(RQ_\mathrm{s})^{-2}$, where R is the transverse radius of the collision zone.

This explains the existence of a long range correlation in rapidity between pairs of particles, but not why their correlation is strongly peaked in azimuthal angle. The 2-gluon correlation one gets from the CGC color fields is nearly independent of the azimuthal angle, because, on average, these gluons can be emitted in any transverse direction. However, one should keep in mind that the above causality argument applies only to the correlation in rapidity, not to the correlation in azimuthal angle that may well be produced later. The azimuthal correlation can be generated by the radial flow [66, 67] that develops subsequently and expels radially the matter produced in heavy ion collisions. Simple relativistic kinematics indeed shows that if one boosts a 2-particle spectrum independent of azimuth, it becomes peaked around $\Delta\phi = 0$ (the prominence of the peak increases with the velocity of the boost) [64].

In Fig. 24, we show a comparison of the strength of the azimuthal correlation in data and in a very simple radial boost model where a unique radial boost velocity is applied to a flat spectrum (the radial velocity is estimated from the slope of $p_\perp$ spectra a small momentum). The centrality dependence, that in this model comes from the increase of the radial velocity with centrality, is in fair qualitative agreement with the measurement.

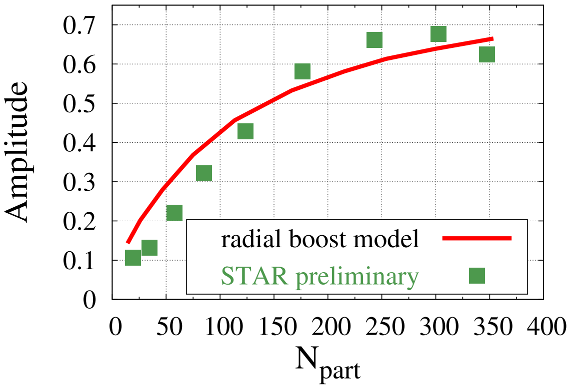

Fig. 24. Comparison of the strength of the azimuthal correlation in data and in a simple radial boost model [68] (see also [69]).

---

[15] The fact that the chromo-electric and chromo-magnetic fields are purely longitudinal at early time does not seem to play any role in this argument. The important properties are their coherence length in rapidity and in the transverse plane.

8. Evolution post collision

8.1. Matching between CGC and hydrodynamics

The CGC provides a self-contained QCD based framework for describing heavy ion collisions from first principles. It also provides tools for calculating inclusive observables at leading log accuracy, *i.e.* leading order plus a resummation of all the leading log contributions coming from higher loop diagrams. However, there is some physics that plays an important role in heavy ion collisions but is not included in the CGC. The fact that the produced gluons and quarks will eventually hadronize when their energy density falls below the QCD critical energy density is obviously not present in the CGC.

For this reason, the CGC can only describe the early stages of the fireball expansion, and should be later on matched onto another description such as relativistic hydrodynamics [70–77]. Since the components of the energy momentum tensor can be computed in the CGC framework, one could use it as initial data for the hydrodynamical evolution. Firstly, for such a matching to be possible, the CGC must bring the system to a state that hydrodynamics can handle. This means that the transverse and longitudinal pressure should not be too different (in particular, the longitudinal pressure should not be negative), and that the viscous effects (*e.g.* the ratio η/s of the shear viscosity to the entropy density) should be small.

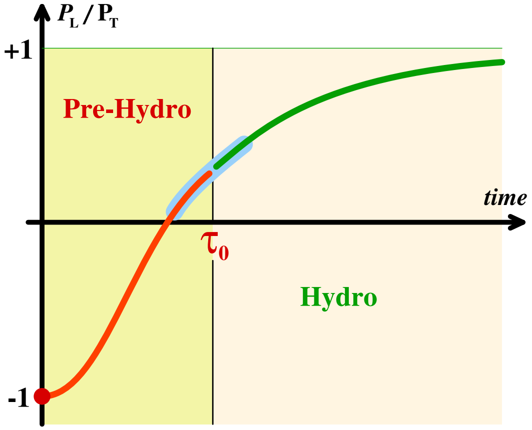

Fig. 25. Smooth matching between CGC and hydrodynamics.

Moreover, when performing such a matching between two descriptions that use different degrees of freedom, one should be careful to check that the two descriptions are compatible in a certain time window. In other words, there should be some range where the two models will predict equivalent results. If this is the case, the time τ_0 at which the matching is realized is not important, and it can be varied in this range without any incidence on the final result[16] (see Fig. 25).

The typical behavior of the ratio η/s in a gauge theory in equilibrium is shown in Fig. 26. When the coupling is small, this ratio can be calculated in a weak coupling expansion. For QCD, it is given by

$$\frac{\eta}{s} \approx \frac{5.1}{g^4 \ln\left(\frac{2.4}{g}\right)} \,. \tag{41}$$

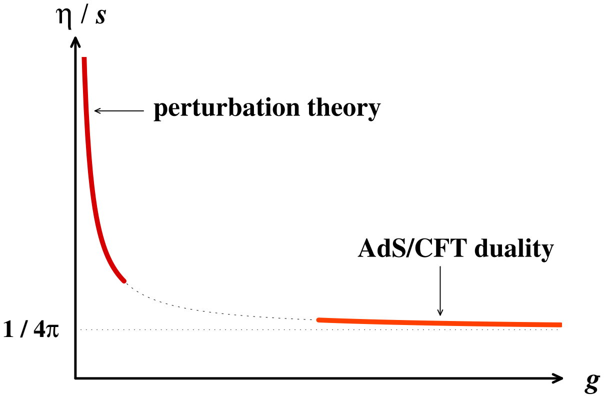

Fig. 26. Shear viscosity to entropy ratio in a gauge theory as a function of the coupling.

This formula shows that η/s is large at weak coupling. At large coupling, this quantity cannot be calculated in QCD, but there is an exact result for a supersymmetric cousin of QCD, the $N = 4$ SUSY Yang–Mills theory[17]: $\eta/s = 1/(4\pi)$ [78, 79]. From this plot, it seems that only strongly coupled systems can have a small η/s ratio. There is, however, a possibility to evade this conclusion. Firstly, one should recall the kinetic interpretation of the ratio η/s

$$\frac{\eta}{s} \sim \frac{\text{mean free path}}{\text{de Broglie wavelength}} \,. \tag{42}$$

---

[16] This is very similar to the factorization of the source distribution $W[\rho]$ in the calculation of inclusive observables. The independence with respect to the cutoff $y_{\rm cut}$ is possible because the static sources describe the same physics as the gauge fields in a certain range of longitudinal momentum.

[17] This gauge theory is conformal, and is dual to a string theory in an $\mathrm{AdS}_5\times\ \mathrm{S}_5$ background. The large coupling limit of the gauge theory corresponds to the weak coupling limit of the string theory, in which gravity becomes classical and reduces to Einstein's equations.

In a system where the degrees of freedom have a typical momentum Q, the de Broglie wavelength is of the order of Q^{-1}, while the inverse mean free path is given by

$$(\text{mean free path})^{-1} \sim \underbrace{g^4 Q^{-2}}_{\text{cross section}} \times \underbrace{\int_{\boldsymbol{k}} f_{\boldsymbol{k}}}_{\text{density}} \underbrace{(1+f_{\boldsymbol{k}})}_{\substack{\text{Bose}\\ \text{enhancement}}} . \tag{43}$$

The factor $1+f_{\boldsymbol{k}}$ under the integral is not needed when discussing dilute plasmas, but is important if the occupation number is large. In the CGC, just after the collision of two heavy ions, one has $f_{\boldsymbol{k}} \sim g^{-2}$ up to $k \sim Q$. Therefore, in such a system, one has $\eta/s \sim g^0$, which is much smaller than the perturbative result in equilibrium. It seems, therefore, plausible that the strong color fields produced in heavy ion collisions may flow, not because they are strongly coupled but because they are highly occupied.

The other main feature of heavy ion collisions is the very rapid expansion of the system in the longitudinal expansion, which causes a redshifting of the longitudinal momenta. As illustrated in Fig. 27, this makes the pressure tensor anisotropic. The figure shows what the expansion does on non-interacting particles. Starting from a nearly isotropic distribution of the velocities at the time τ_1, the expansion will "filter" the particles so that at the time τ_2 only particles with the momentum rapidity $y \approx \eta$ exist at the space-time rapidity η. This means that, in the local comoving frame, the longitudinal pressure is much smaller than the transverse one. This anisotropy, if it becomes too large, is a problem for hydrodynamics. Indeed, the difference between the two pressures goes into the viscous terms[18], and if they are large hydrodynamics may incorrectly reproduce the underlying dynamics.

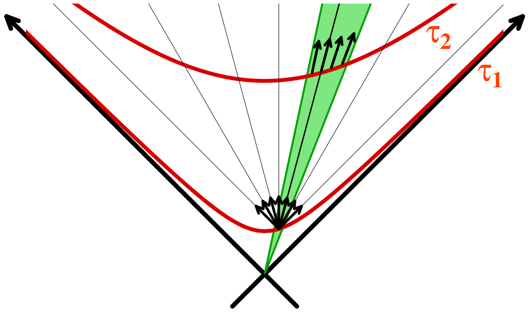

Fig. 27. Role of the expansion in decreasing the longitudinal pressure.

---

[18] There are now attempts to view hydrodynamics as an expansion around a non-isotropic background. In this formulation, this may be less of a problem [80–86].

Let us now discuss the CGC prediction for the energy momentum tensor, starting with the LO calculation[19]. Immediately after the collision, at $\tau = 0^+$, it is known analytically that the chromo-electric and chromo-magnetic fields are both parallel to the collision axis. This structure of the color fields implies that the energy momentum tensor is diagonal, with[20] $P_{\rm T} = \epsilon$ and $P_{\rm L} = -\epsilon$. At later times, the energy-momentum tensor must be determined numerically by solving the classical Yang–Mills equations, and by computing $T^{\mu\nu}$ from the classical gauge fields. The results of this calculation [37, 87] are shown in Fig. 28. After starting at -1, the ratio $P_{\rm L}/\epsilon$ increases and becomes mostly positive at a time of the order of $Q_{\rm s}\tau \sim 1$. However, this calculation shows that the longitudinal pressure remains at all times much smaller than the transverse one. Thus, the CGC at leading order seems to lead to a situation which is similar to free streaming. This leads to an unsatisfactory matching between the CGC at LO and hydrodynamics[21].

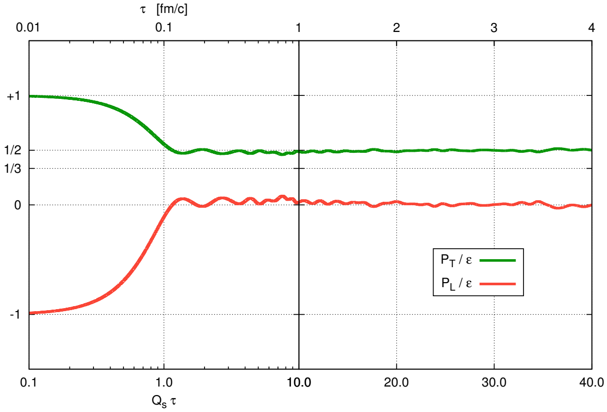

Fig. 28. Transverse and longitudinal pressure to energy density ratios, in the CGC at leading order.

---

[19] This discussion also applies to the LO result improved by the resummation of the leading log corrections. This does not change the conclusion of this paragraph since this resummation is totally absorbed into the rapidity evolution of the distributions $W[\rho]$.

[20] The negative longitudinal pressure in a longitudinal flux tube is the analogue of a string tension.

[21] In principle, this matching requires several steps: (1) compute $T^{\mu\nu}$ from CGC, (2) find the time-like eigenvector such that $u_\mu T^{\mu\nu} = \epsilon u^\nu$ (this defines the local rest frame, and the energy density), (3) compute the pressure from some equation of state $P = f(\epsilon)$, (4) compute the viscous stress tensor as the difference between the full $T^{\mu\nu}$ and the ideal part (obtained from ϵ, P and u^μ). In many calculations using "CGC initial conditions", a simplified procedure is often employed, where one assumes that $u^\mu = (1, \mathbf{0})$: (1) compute $\epsilon = T^{00}$, (2) define $P = f(\epsilon)$, (3) neglect the viscous stress tensor.

Indeed, in hydrodynamics the ratio $P_{\rm L}/P_{\rm T}$ increases to approach 1, while it remains near zero in the CGC at LO (see Fig. 29).

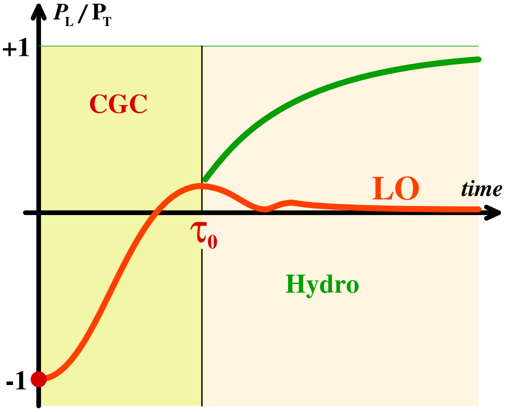

Fig. 29. Matching between hydrodynamics and the CGC at LO.

8.2. Weibel instability

There is, however, a good reason to explore the CGC beyond leading order. Indeed, the boost invariant solutions of the classical Yang–Mills equations are unstable [87–96]. When their initial condition is modified by a small but rapidity dependent perturbation, the solution diverges from the unperturbed one. This is illustrated in Fig. 30, that shows a component of the energy momentum tensor that should be very small at all times if the perturbation is stable. Instead, it growths like the exponential[22] of $\sqrt{\tau}$ (over a characteristic timescale of the order of Q_s^{-1}). These unstable modes in the classical Yang–Mills equations are closely related to the Weibel instability that occurs in anisotropic plasmas in QED and in QCD [97–118]. More details on how these instabilities of the classical solutions develop can be found in Refs. [87, 94, 95, 119].

These instabilities force us to reconsider the power counting that was the basis for organizing the expansion in powers of g^2 of inclusive observables. As we have seen before, the 1-loop corrections — that are formally of the relative order of g^2 — contain leading log terms proportional to the cutoff $y_{\rm cut}$, that can be absorbed into a redefinition of the distributions $W[\rho]$. Because of the instabilities, the 1-loop correction also contain some terms that grow exponentially in time. Eventually, the size of these exponential factors will compensate the g^2 that comes from the loop, and these terms

---

[22] The fact that $\sqrt{\tau}$ appears here instead of τ itself is due to the longitudinal expansion of the system. Because of the expansion, the equation that drives the growth of the perturbations is a Bessel equation instead of an ordinary wave equation.

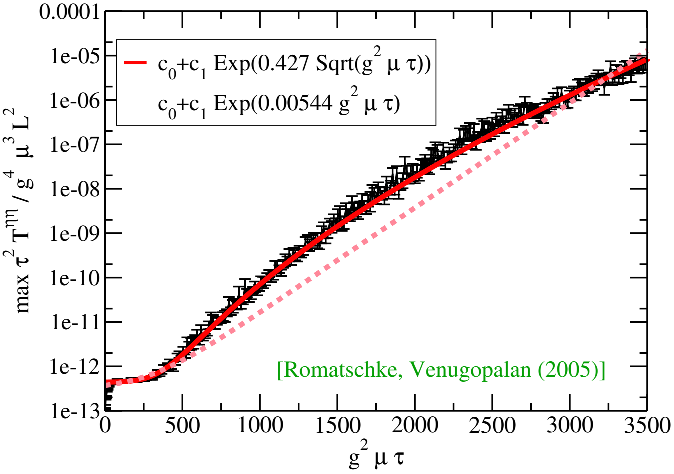

Fig. 30. Growth of unstable modes in classical Yang–Mills dynamics.

will be as large as the LO terms. This statement is illustrated in Fig. 31, where we compare the energy density and pressure at LO and LO+NLO in a ϕ^4 scalar field theory [120], in which the solutions of the classical field equations of motion are also unstable[23]. This computation shows clearly that the fixed order LO+NLO result cannot be trusted after some time, because it becomes much larger than the LO result (note that this happens only for the pressure, because the energy density is protected from this exponential growth by energy conservation).

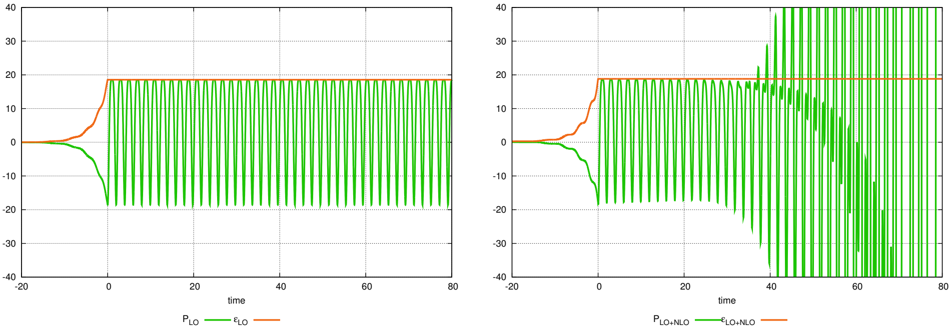

Fig. 31. Effect of parametric instabilities on the perturbative expansion of the energy-momentum tensor in a scalar ϕ^4 theory.

---

[23] The instability in the ϕ^4 theory is of a totally different nature, since it is caused by parametric resonance. However, the detailed mechanism of the instability is not important in this discussion.

Although a similar NLO calculation has not been done in the CGC, one can guess what would happen. The Weibel instabilities would produce an unbound growth of the longitudinal pressure, and this time the ratio $P_{\rm L}/P_{\rm T}$ would be driven to arbitrarily large values exceeding unity. Attempting to match such a NLO CGC initial condition to hydrodynamics would not be better than at LO, as illustrated in Fig. 32.

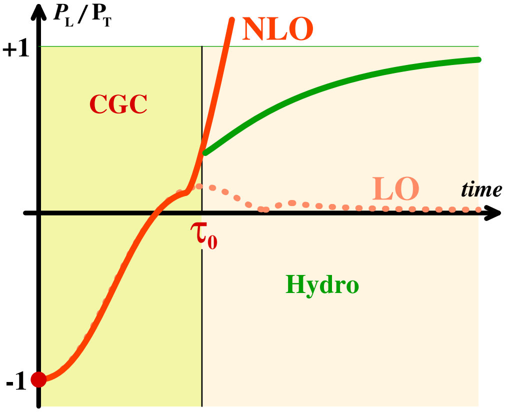

Fig. 32. Matching between hydrodynamics and the CGC at NLO.

8.3. Resummation of the leading terms

The same problem would, in fact, occur at any fixed loop order. The only way to improve the situation is to examine each loop order and to resum the most important terms at each order. For this, we need first to modify the power counting rules that we have established earlier, in order to keep track of the unstable modes. Let us first examine the graph that contributes at 1-loop, represented in the top-left corner of Fig. 33, in conjunction with the formula (32). In this formula, each of the derivatives with respect to the initial classical field creates a perturbation to this classical field, that we have indicated by light gray/green propagators in Fig. 33 (in the top-left graph, only the term proportional to Γ_2, that has second derivatives with respect to the initial fields, has been represented — the term with only one derivative has a slower growth with time). The "standard" power counting would assign a factor g^2 to the loop and a factor $1/g$ to each of the derivatives $\partial/\partial\mathcal{A}_{\rm init}$ (represented by a gray/blue dot in the graphs). Thus, the NLO correction to the energy-momentum tensor is expected to be of the order of g^0, while the LO is of the order of g^{-2}. From this diagrammatic representation, it is also easy to count the number of perturbations of the classical field. Each of them will develop into a factor of the order of $\exp(\sqrt{\mu\tau})$ (μ is of the order

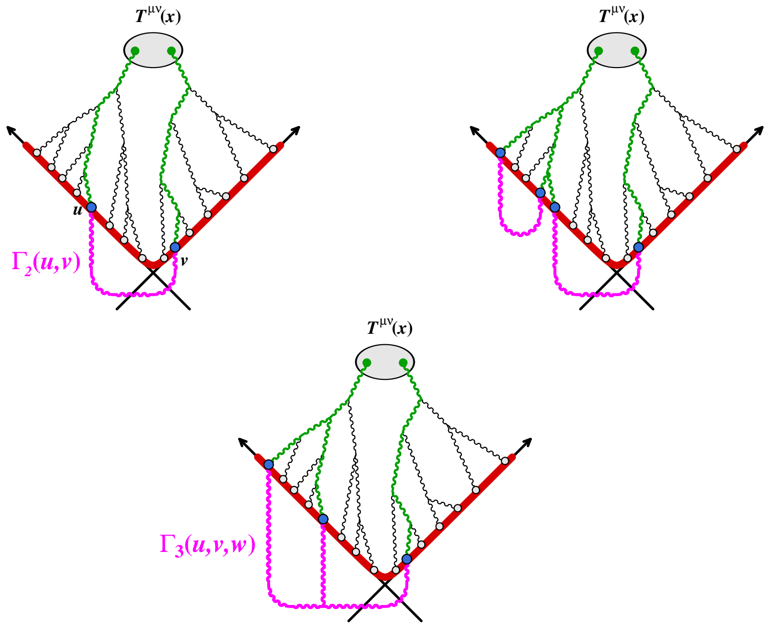

Fig. 33. Improved power counting taking into account the growth of the unstable modes.

of $Q_{\rm s}$). Thus, the expansion of $T^{\mu\nu}$ is more accurately written[24] as

$$T^{\mu\nu} = c_0\, g^{-2} + c_1\, g^0\, e^{2\sqrt{\mu\tau}} + \dots\,, \tag{44}$$

where the coefficients c_0, c_1 do not grow exponentially with time. From this pocket formula, one can deduce at which time the naive loop expansion breaks down. This is the time when the 1-loop result becomes as large as the leading order, *i.e.*

$$\tau_{\rm max} \sim \mu^{-1} \log^2\left(1/g^2\right)\,. \tag{45}$$

Up to a logarithmic factor, this time is of the order of the inverse saturation momentum.

At two loops, the naive power counting tells us that we should get terms of the order of g^2. However, not all the terms have the same growth in time. In Fig. 33, we have represented two types of 2-loop contributions in order to illustrate these differences. In the top-right graph, the two loops are the seed of four perturbations to the classical field, while in the bottom graph,

---

[24] This formula indicates the worst possible behavior. It is possible that some components of the energy-momentum tensor will not be affected by the instability, as was the case in the scalar field theory considered in Fig. 31.

only three of these perturbations are created. The latter term will, therefore, have a subleading time behavior. Moreover, one sees that the distinguishing feature of the top-right graphs is that it can be generated by acting twice with the quadratic part of the operator that appears in Eq. (32). This reasoning extends to all orders. At the $n^{\rm th}$ loop order, the maximal number of field perturbations is $2n$, and the corresponding graphs are generated by acting n times with this operator. Formally, the sum of all these leading terms can be obtained by

$$T^{\mu\nu}_{\rm resummed} \equiv \exp\left[\frac{1}{2}\int_{\boldsymbol{u},\boldsymbol{v}} \boldsymbol{\Gamma}_2(\boldsymbol{u},\boldsymbol{v})\frac{\partial}{\partial\mathcal{A}_{\rm init}(\boldsymbol{u})}\frac{\partial}{\partial\mathcal{A}_{\rm init}(\boldsymbol{v})}\right] T^{\mu\nu}_{\rm LO}\,. \qquad (46)$$

Note that the Taylor coefficients of the exponential correspond precisely to the symmetry factors of graphs such as the top-right diagram of Fig. 33. Moreover, since the 2-point function $\boldsymbol{\Gamma}_2$ is precisely the one that appears in the NLO result, one has

$$T^{\mu\nu}_{\rm resummed} = T^{\mu\nu}_{\rm LO} + T^{\mu\nu}_{\rm NLO} + \ldots \qquad (47)$$

In other words, this resummation includes in full the LO and NLO contributions, and a subset of all the higher loop contributions. It is important to keep in mind that, starting at the 2-loop order, it is an approximation and is not equivalent to the complete underlying theory. This will have important consequences that we will discuss in the next section.

9. Classical statistical approximation

9.1. Reformulation as a Gaussian average

At this point, the resummation performed via Eq. (46) is quite formal. Three questions must be addressed: (1) can this formula in terms of functional derivatives be evaluated numerically? (2) does Eq. (46) lead to results whose time dependence is bounded? (3) when doing this, are we introducing other pathologies?

In order to answer the first question, one should recall the following identity

$$e^{\frac{\alpha}{2}\partial_x^2}\, f(x) = \int_{-\infty}^{+\infty} dz\, \frac{e^{-z^2/2\alpha}}{\sqrt{2\pi\alpha}}\, f(x+z)\,. \qquad (48)$$

This formula can be established *e.g.* by applying a Fourier transform to both sides. Although we cast it here in a space of functions of a single variable, this formula can be generalized to operators that are Gaussian in derivatives in a functional space. It enables us to rewrite Eq. (46) as[25]

$$T^{\mu\nu}_{\text{resummed}} = \int [Da]\, \exp\left[-\frac{1}{2}\int_{\boldsymbol{u},\boldsymbol{v}} a(\boldsymbol{u})\boldsymbol{\Gamma}_2^{-1}(\boldsymbol{u},\boldsymbol{v})a(\boldsymbol{v})\right] T^{\mu\nu}_{\text{LO}}[\mathcal{A}_{\text{init}}+a]\,. \quad (49)$$

This resummation procedure, where one averages classical trajectories over an ensemble of initial conditions, is known as the *Classical Statistical Approximation* (CSA).

From this equation, one can easily see that the problem of the unbounded growth of the fluctuations has been cured. Indeed, this resummation has promoted the linearized perturbations[26] into an integral part of the non-linear classical field (the initial condition of the classical field is modified by the perturbation, but its evolution remains fully non-linear). In any theory where the potential prevents the fields from running away to infinity, this guarantees that this resummed quantity will not diverge in time.

9.2. Practical implementation

In the form of Eq. (49), the procedure for evaluating the resummed energy-momentum tensor[27] is quite straightforward:

1. Determine the 2-point function $\boldsymbol{\Gamma}_2(\boldsymbol{u},\boldsymbol{v})$ that defines the Gaussian fluctuations, for the initial time $Q_s\tau_0$ of interest. This is an initial value problem, whose outcome is uniquely determined by the state of the system at $x^0 = -\infty$, and depends on the history of the system from $x^0 = -\infty$ to $\tau = \tau_0$. This problem is solvable analytically as long as the fluctuations remain weak, $a^\mu \ll Q_s/g$. After that, the fluctuations start to interact non-linearly, and their spectrum becomes non-Gaussian. This imposes the initial time to be chosen such that $Q_s\tau_0 \ll 1$.
2. Solve the classical Yang–Mills equations from τ_0 to τ_f. In high energy collisions, the problem as a whole is boost invariant, but individual field configurations are now rapidity dependent because of the fluctuating part superimposed to their initial condition. Therefore, unlike in the CGC at LO, the classical Yang–Mills equations must be solved in 3+1 dimensions.
3. Do a Monte-Carlo sampling of the fluctuating initial conditions.

---

[25] Such a Gaussian averaging procedure has also been used in other fields [121–125].

[26] One would recover the pathological behavior of the NLO result by linearizing the equation of motion for the classical field of initial condition $\mathcal{A}_{\text{init}} + a$.

[27] Although the discussion here is centered on the energy-momentum tensor, the same resummation can be applied to any inclusive quantity.

The setup for doing this is the same as the one described when discussing the CGC at LO. One must discretize the classical Yang–Mills equations in the system of coordinates $\tau, \eta, \boldsymbol{x}_\perp$. Therefore, the lattice used in these computations represents a sub-volume of the interaction region that expands in the longitudinal direction, as illustrated in Fig. 34. This implies that the lattice spacing in the z coordinate is time dependent. In order to be able to resolve the physically relevant scales at the final time τ_f of the simulation, it is usually necessary to have a larger number of lattice spacings in the longitudinal direction.

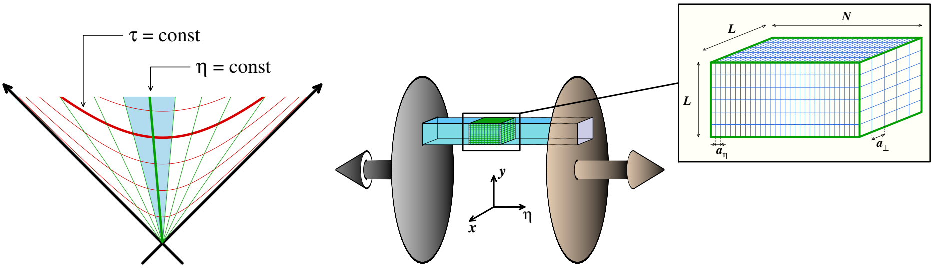

Fig. 34. Lattice setup for numerical implementations of the classical statistical method.

9.3. Initial conditions

Let us say a few words about the calculation of the variance $\boldsymbol{\Gamma}_2$ of the initial fluctuations that were used in Ref. [126]. In the CGC[28], the initial Gaussian ensemble of fields is characterized by the following mean values and variance (written here in very sketchy way, without color and Lorentz indices):

---

[28] Note that the same method can be used with a spectrum of initial conditions not derived from the CGC [127–130]. For instance, one may choose a Gaussian distribution of zero mean, and whose variance corresponds to a distribution of free particles

$$\left\langle \mathcal{A}^\mu \right\rangle = 0\,, \qquad \boldsymbol{\Gamma}_2(\boldsymbol{u},\boldsymbol{v}) = \int\limits_{\text{modes } \boldsymbol{k}} f_0(\boldsymbol{k})\; a_{\boldsymbol{k}}(\boldsymbol{u}) a^*_{\boldsymbol{k}}(\boldsymbol{v})\;, \qquad a_{\boldsymbol{k}}(x) \equiv e^{ik\,x}\,.$$

If one recalls the symmetric 2-point Green's function in the Schwinger–Keldysh formalism in the presence of a bath of particles,

$$G_S(k) = 2\pi \left(\tfrac{1}{2} + f(\boldsymbol{k})\right) \delta\left(k^2\right)\,,$$

it appears that the initial CGC fluctuations in Eqs. (50) are vacuum fluctuations (the 1/2 in the previous formula) rather than quasiparticles.

$$\begin{aligned}
&\big\langle\mathcal{A}^\mu\big\rangle = \mathcal{A}^\mu_{\rm LO}\,,\\
&\boldsymbol{\Gamma}_2(\boldsymbol{u},\boldsymbol{v}) = \tfrac12 \int\limits_{\text{modes }\boldsymbol{k}} a_{\boldsymbol{k}}(\boldsymbol{u})a^*_{\boldsymbol{k}}(\boldsymbol{v})\,,\\
&\Big[\mathcal{D}_\rho\mathcal{D}^\rho\delta_\mu^\nu - \mathcal{D}_\mu\mathcal{D}^\nu + ig\,\mathcal{F}_\mu{}^\nu\Big]a^\mu_{\boldsymbol{k}} = 0\,,\\
&\lim_{x^0\to-\infty} a_{\boldsymbol{k}}(x) = e^{ik\,x}\,.
\end{aligned}\qquad (50)$$

The mean value is already known from the LO calculation [26]. The formula for the variance comes from the derivation of the NLO contribution. In order to evaluate it, we need to solve the third of Eqs. (50), that describes the evolution of a small perturbation on top of the LO classical background color field [131]. This evolution equation must be solved from $x^0 = -\infty$, where the initial condition is a plane wave of momentum $\boldsymbol{k}$, to the time τ_0 (in the forward light-cone) at which the numerical simulation will start (left-hand side of Fig. 35). As long as we stay in a regime where these perturbations are not yet enhanced by instabilities, the variance is small compared to the mean value squared, and this Gaussian distribution is a narrow distribution centered on the LO color fields (see the right-hand side of Fig. 35).

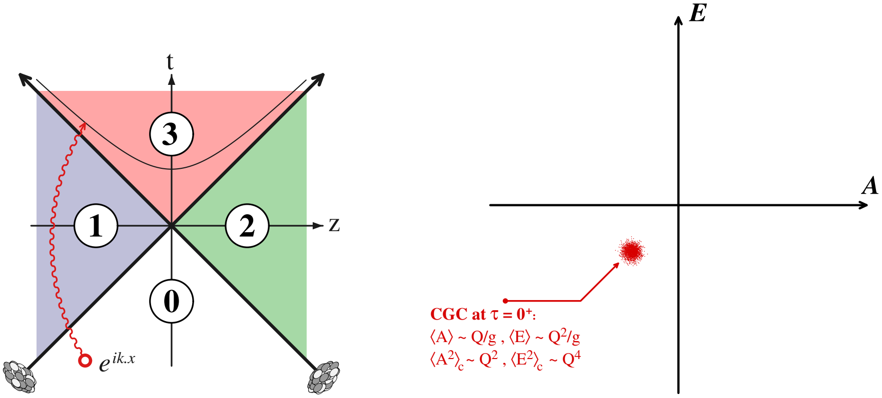

Fig. 35. CGC spectrum of initial fluctuations at $Q_s\tau_0 \ll 1$.

9.4. Quantum mechanical analogue

The Classical Statistical Approximation has an analogue in ordinary quantum mechanics, which is helpful to understand what approximation is being made when one uses it. Consider the von Neumann equation for the time evolution of the density operator of a quantum system

$$\frac{\partial \widehat{\rho}_\tau}{\partial \tau} = i\,\hbar\,\left[\widehat{H}, \widehat{\rho}_\tau\right]\,. \tag{51}$$

By performing a Wigner transformation,

$$\begin{aligned} W_\tau(\boldsymbol{x},\boldsymbol{p}) &\equiv \int d\boldsymbol{s}\; e^{i\boldsymbol{p}\,\boldsymbol{s}}\; \left\langle \boldsymbol{x}+\frac{\boldsymbol{s}}{2}\right| \widehat{\rho}_\tau \left|\boldsymbol{x}-\frac{\boldsymbol{s}}{2}\right\rangle\,, \\ \mathcal{H}(\boldsymbol{x},\boldsymbol{p}) &\equiv \int d\boldsymbol{s}\; e^{i\boldsymbol{p}\,\boldsymbol{s}}\; \left\langle \boldsymbol{x}+\frac{\boldsymbol{s}}{2}\right| \widehat{H} \left|\boldsymbol{x}-\frac{\boldsymbol{s}}{2}\right\rangle \;\text{(classical Hamiltonian)}\,, \end{aligned} \tag{52}$$

Eq. (51) can be rewritten as follows,

$$\begin{aligned} \frac{\partial W_\tau}{\partial \tau} &= \frac{2}{i\,\hbar}\,\mathcal{H}(\boldsymbol{x},\boldsymbol{p})\,\sin\left(\frac{i\,\hbar}{2}\left(\overleftarrow{\partial}_{\boldsymbol{p}}\overrightarrow{\partial}_{\boldsymbol{x}} - \overleftarrow{\partial}_{\boldsymbol{x}}\overrightarrow{\partial}_{\boldsymbol{p}}\right)\right)\,W_\tau(\boldsymbol{x},\boldsymbol{p}) \\ &= \underbrace{\left\{\mathcal{H}, W_\tau\right\}}_{\text{Poisson bracket}} + \mathcal{O}\left(\hbar^2\right)\,. \end{aligned} \tag{53}$$

The first line is still exact. In the second line, one has performed an expansion in powers of $\hbar$ in which only the first non-vanishing term is kept. Since this leading order term is nothing but the classical Poisson bracket, the function W_τ obeys the Liouville equation in this approximation. In other words, the system evolves classically. Moreover, since the sine is an odd function, the first neglected term comes only at the order $\hbar^2$. This is equivalent to the fact that the CSA in quantum field theory agrees with the full theory at LO and NLO, and starts to miss some terms at two loops. It is important to note that this does not mean that $\mathcal{O}(\hbar)$ effects are absent; but such effects can only come via the initial condition, and therefore they can be taken into account in this approximation. In fact, since in quantum mechanics one cannot assign definite values to $\boldsymbol{x}$ and $\boldsymbol{p}$ at the same time, there is a natural $\hbar$ dependence coming from the spread of the initial conditions, $\boldsymbol{\Delta x}\cdot\boldsymbol{\Delta p} \geq \hbar$.

9.5. Ultraviolet divergences and non-renormalizability

In quantum field theory, it is instructive to see how the CSA can be derived from the path integral formalism in the Schwinger–Keldysh formalism

$$\left\langle \mathcal{O}\right\rangle = \int \left[D\phi_+ D\phi_-\right]\,\mathcal{O}\left[\phi_\pm\right]\,e^{i(S[\phi_+]-S[\phi_-])}\,. \tag{54}$$

In this equation, ϕ_+ can be viewed as the field in the amplitude, ϕ_- is the field in the conjugate amplitude, and their difference $\phi_+ - \phi_-$ results from quantum interferences. Let us introduce $\phi_1 \equiv \phi_+\phi_-$ and $\phi_2 \equiv \frac{1}{2}(\phi_+ + \phi_-)$.

In terms of these new fields, the action can be rewritten as

$$S[\phi_+] - S[\phi_-] = \phi_1 \, \frac{\delta S[\phi_2]}{\delta \phi_2} + \text{terms cubic in } \phi_1 \,. \tag{55}$$

In the strong field regime, $\phi_\pm$ are large, but $\phi_+ - \phi_-$ is small. Therefore, we may neglect the terms that are cubic in ϕ_1, and we see that the functional integration over ϕ_1 leads to the classical Euler–Lagrange equations for ϕ_2. The only remaining fluctuations are in the initial condition for ϕ_2.

The main advantage of this alternate derivation of the CSA is that it provides us a way to study its consequences perturbatively, order by order in g^2. After going from the fields $\phi_\pm$ to $\phi_{1,2}$, one obtains Feynman rules (sometimes called the retarded-advanced formalism) that have two kinds of vertices 1222 and 1112 (for a ϕ^4 scalar theory). This is a consequence of the fact that the action in Eq. (55) is odd in ϕ_1. The CSA is equivalent to neglecting the 1112 vertex. By this method, it has been realized recently that the CSA is a non-renormalizable approximation of the underlying quantum field theory. For instance, for the self-energy Σ_{12} at two loops (for a ϕ^4 scalar field theory), the CSA gives an ultraviolet divergent result

Im 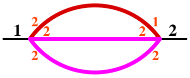 $= -\dfrac{g^4}{1024\pi^3}\left(\Lambda_{\mathrm{UV}}^2 - \dfrac{2}{3}p^2\right) . \qquad (56)$

Since this divergence occurs in the imaginary part of a correlator, it cannot be removed by a counterterm added to the action (otherwise that would make the action non-Hermitian). The consequence of this is that one cannot take the continuum limit in computations based on the CSA. However, when the ultraviolet cutoff is chosen not too large compared to the physical scales, the CSA can provide a good qualitative and semi-quantitative description of the evolution of the system.

9.6. Vacuum fluctuations and isotropization

Note that this non-renormalizability problem arises only when one uses the CSA in conjunction with a spectrum of initial conditions that represents vacuum fluctuations, as in Eqs. (50). When using particle-like initial conditions, such as those described in the footnote 28, the CSA is ultraviolet finite provided that the initial particle distribution falls faster than $1/k$. Because of this, if one forgets that this type of initial condition is not derived from the CGC, this implementation of the CSA may seem better since one does not need to worry about the dependence on the ultraviolet cutoff.

However, this choice of initial conditions in the CSA may be inadequate in order to study the problem of isotropization in heavy ion collisions, for the following reason. For the purpose of this argument, let us reason in terms of the corresponding Boltzmann equation. For 2 → 2 collisions, it reads

$$\partial_t f_3 \sim g^4 \int\limits_{124} \dots [f_1 f_2 (f_3 + f_4) - f_3 f_4 (f_1 + f_2)] + g^4 \int\limits_{124} \dots [f_1 f_2 - f_3 f_4] \,. \tag{57}$$

(Here, we are tracking the distribution of particles of momentum k_3 — see Fig. 36.) In this equation, we have separated the purely classical terms (in f^3) from the subleading f^2 terms. When only particle-like fluctuations are included, the CSA gives only the f^3 terms, and drops all the other terms. In contrast, the CSA where vacuum fluctuations are included has the f^3 and f^2 terms, and also some spurious terms that are linear in f (these spurious terms are closely related to the fact that this version of the CSA is non-renormalizable).

Consider now a situation where the particle distribution is extremely anisotropic, with a support in k_z which is extremely squeezed compared to the support in $\boldsymbol{k}_\perp$. Starting from this kind of initial condition, the unapproximated Boltzmann equation would lead to isotropization because two purely transverse particles can be scattered outside of the transverse plane. But does this still happen in approximations of the Boltzmann equation? In Fig. 36, one has $k_3^z = -k_4^z \neq 0$, and given our assumption about the support of the particle distribution, this means that $f_3 = f_4 \approx 0$. In the collision

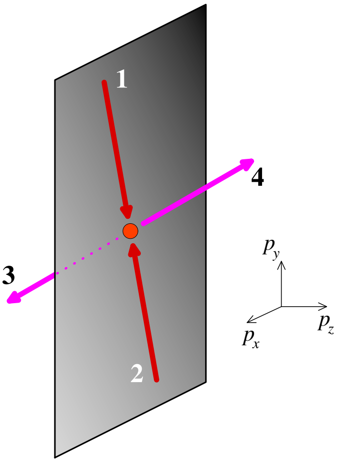

Fig. 36. 2 → 2 scattering contributing to isotropization.

term of the Boltzmann equation, a number of terms therefore vanish

$$\begin{aligned}\partial_t f_3 \sim g^4 \int\limits_{124} \ldots \left[f_1 f_2 (\underbrace{f_3 + f_4}_{0}) - \underbrace{f_3 f_4}_{0} (f_1 + f_2) \right] \\ + g^4 \int\limits_{124} \ldots \left[f_1 f_2 - \underbrace{f_3 f_4}_{0} \right] .\end{aligned} \tag{58}$$

In particular, all the cubic terms are zero. The problem is that these are the only terms that are kept in the CSA with no vacuum fluctuations. The only non-zero term is the term in $f_1 f_2$, which would be present in the version of the CSA that uses vacuum initial fluctuations. From this discussion, the particle-like initial conditions in the CSA, despite their appeal since they lead to UV finite results, may be inappropriate because they lead to missing the most important contribution to isotropization.

This work is supported by the Agence Nationale de la Recherche project 11-BS04-015-01.

REFERENCES

[1] F.D. Aaron *et al.* [H1 and ZEUS collaborations], *J. High Energy Phys.* **1001**, 109 (2010).

[2] G. Altarelli, G. Parisi, *Nucl. Phys.* **B126**, 298 (1977).

[3] V.N. Gribov, L.N. Lipatov, *Sov. J. Nucl. Phys.* **15**, 438 (1972).

[4] V.N. Gribov, L.N. Lipatov, *Sov. J. Nucl. Phys.* **15**, 675 (1972).

[5] Yu. Dokshitzer, *Sov. Phys. JETP* **46**, 641 (1977).

[6] L.V. Gribov, E.M. Levin, M.G. Ryskin, *Phys. Rep.* **100**, 1 (1983).

[7] A.H. Mueller, J-W. Qiu, *Nucl. Phys.* **B268**, 427 (1986).

[8] J.P. Blaizot, A.H. Mueller, *Nucl. Phys.* **B289**, 847 (1987).

[9] I. Balitsky, L.N. Lipatov, *Sov. J. Nucl. Phys.* **28**, 822 (1978).

[10] E.A. Kuraev, L.N. Lipatov, V.S. Fadin, *Sov. Phys. JETP* **45**, 199 (1977).

[11] A. Deshpande, R. Ent, R. Milner, CERN Courier, October 2009.

[12] E. Iancu, R. Venugopalan, *Quark Gluon Plasma 3*, Eds. R.C. Hwa, X.N. Wang, World Scientific [`arXiv:hep-ph/0303204`].

[13] T. Lappi, *Int. J. Mod. Phys.* **E20**, 1 (2011).

[14] H. Weigert, *Prog. Part. Nucl. Phys.* **55**, 461 (2005).

[15] F. Gelis, E. Iancu, J. Jalilian-Marian, R. Venugopalan, *Annu. Rev. Part. Nucl. Sci.* **60**, 463 (2010).

[16] L.D. McLerran, R. Venugopalan, *Phys. Rev.* **D49**, 2233 (1994).

[17] L.D. McLerran, R. Venugopalan, *Phys. Rev.* **D49**, 3352 (1994).

[18] L.D. McLerran, R. Venugopalan, *Phys. Rev.* **D50**, 2225 (1994).

[19] F. Gelis, R. Venugopalan, *Nucl. Phys.* **A776**, 135 (2006).

[20] F. Gelis, R. Venugopalan, *Nucl. Phys.* **A779**, 177 (2006).

[21] J. Schwinger, *J. Math. Phys.* **2**, 407 (1961).

[22] L.V. Keldysh, *Sov. Phys. JETP* **20**, 1018 (1964).

[23] R.E. Cutkosky, *J. Math. Phys.* **1**, 429 (1960).

[24] G. 't Hooft, M.J.G. Veltman, CERN report 73-9.

[25] Yu.V. Kovchegov, *Phys. Rev.* **D54**, 5463 (1996).

[26] A. Kovner, L.D. McLerran, H. Weigert, *Phys. Rev.* **D52**, 6231 (1995).

[27] A. Krasnitz, R. Venugopalan, *Nucl. Phys.* **B557**, 237 (1999).

[28] A. Krasnitz, R. Venugopalan, *Phys. Rev. Lett.* **84**, 4309 (2000).

[29] A. Krasnitz, R. Venugopalan, *Phys. Rev. Lett.* **86**, 1717 (2001).

[30] A. Krasnitz, Y. Nara, R. Venugopalan, *Phys. Rev. Lett.* **87**, 192302 (2001).

[31] A. Krasnitz, Y. Nara, R. Venugopalan, *Nucl. Phys.* **A727**, 427 (2003).

[32] T. Lappi, *Phys. Rev.* **C67**, 054903 (2003).

[33] T. Lappi, *Phys. Lett.* **B643**, 11 (2006).

[34] A. Krasnitz, Y. Nara, R. Venugopalan, *Phys. Lett.* **B554**, 21 (2003).

[35] A. Krasnitz, Y. Nara, R. Venugopalan, *Nucl. Phys.* **A717**, 268 (2003).

[36] T. Lappi, R. Venugopalan, *Phys. Rev.* **C74**, 054905 (2006).

[37] T. Lappi, L.D. McLerran, *Nucl. Phys.* **A772**, 200 (2006).

[38] A. Ayala, J. Jalilian-Marian, L.D. McLerran, R. Venugopalan, *Phys. Rev.* **D53**, 458 (1996).

[39] I. Balitsky, *Phys. Rev.* **D75**, 014001 (2007).

[40] I. Balitsky, G.A. Chirilli, *Phys. Rev.* **D77**, 014019 (2008).

[41] Yu.V. Kovchegov, H. Weigert, *Nucl. Phys.* **A784**, 188 (2007).

[42] E. Gardi, J. Kuokkanen, K. Rummukainen, H. Weigert, *Nucl. Phys.* **A784**, 282 (2007).

[43] A.V. Grabovsky, *J. High Energy Phys.* **1309**, 141 (2013).

[44] A. Kovner, M. Lublinsky, Y. Mulian, *Phys. Rev.* **D89**, 061704 (2014).

[45] A. Kovner, M. Lublinsky, Y. Mulian, `arXiv:1405.0418 [hep-ph]`.

[46] J.L. Albacete *et al.*, *Phys. Rev.* **D71**, 014003 (2005).

[47] J.L. Albacete, Y. Kovchegov, *Phys. Rev.* **D75**, 125021 (2007).

[48] J.L. Albacete, N. Armesto, J.G. Milhano, C.A. Salgado, *Phys. Rev.* **D80**, 034031 (2009).

[49] J.L. Albacete, N. Armesto, J.G. Milhano, C.A. Salgado, `arXiv:0906.2721 [hep-ph]`.

[50] T. Lappi, H. Mäntysaari, *Eur. Phys. J.* **C73**, 2307 (2013).

[51] F. Gelis, T. Lappi, R. Venugopalan, *Phys. Rev.* **D78**, 054019 (2008).

[52] F. Gelis, T. Lappi, R. Venugopalan, *Phys. Rev.* **D78**, 054020 (2008).

[53] F. Gelis, T. Lappi, R. Venugopalan, *Phys. Rev.* **D79**, 094017 (2009).

[54] I. Balitsky, *Nucl. Phys.* **B463**, 99 (1996).

[55] J. Jalilian-Marian, A. Kovner, L.D. McLerran, H. Weigert, *Phys. Rev.* **D55**, 5414 (1997).

[56] J. Jalilian-Marian, A. Kovner, A. Leonidov, H. Weigert, *Nucl. Phys.* **B504**, 415 (1997).

[57] J. Jalilian-Marian, A. Kovner, A. Leonidov, H. Weigert, *Phys. Rev.* **D59**, 014014 (1998).

[58] J. Jalilian-Marian, A. Kovner, A. Leonidov, H. Weigert, *Phys. Rev.* **D59**, 034007 (1999).

[59] J. Jalilian-Marian, A. Kovner, A. Leonidov, H. Weigert, *Phys. Rev.* **D59**, 099903 (1999).

[60] E. Iancu, A. Leonidov, L.D. McLerran, *Nucl. Phys.* **A692**, 583 (2001).

[61] E. Iancu, A. Leonidov, L.D. McLerran, *Phys. Lett.* **B510**, 133 (2001).

[62] E. Ferreiro, E. Iancu, A. Leonidov, L.D. McLerran, *Nucl. Phys.* **A703**, 489 (2002).

[63] B.I. Abelev *et al.* [STAR Collaboration], *Phys. Rev.* **C80**, 064912 (2009).

[64] A. Dumitru, F. Gelis, L. McLerran, R. Venugopalan, *Nucl. Phys.* **A810**, 91 (2008).

[65] T. Lappi, S. Srednyak, R. Venugopalan, *J. High Energy Phys.* **1001**, 066 (2010).

[66] S.A. Voloshin, *Phys. Lett.* **B632**, 490 (2006).

[67] C.A. Pruneau, S. Gavin, S.A. Voloshin, *Nucl. Phys.* **A802**, 107 (2008).

[68] S. Gavin, L. McLerran, G. Moschelli, *Phys. Rev.* **C79**, 051902 (2009).

[69] E.V. Shuryak, *Phys. Rev.* **C76**, 047901 (2007).

[70] J. Adams *et al.* [STAR Collaboration], *Nucl. Phys.* **A757**, 102 (2005).

[71] K. Adcox *et al.* [PHENIX Collaboration], *Nucl. Phys.* **A757**, 184 (2005).

[72] I. Arsene *et al.* [BRAHMS Collaboration], *Nucl. Phys.* **A757**, 1 (2005).

[73] B.B. Back *et al.* [PHOBOS Collaboration], *Nucl. Phys.* **A757**, 28 (2005).

[74] P. Huovinen, P.V. Ruuskanen, *Annu. Rev. Nucl. Part. Sci.* **56**, 163 (2006).

[75] P. Romatschke, *Int. J. Mod. Phys.* **E19**, 1 (2010).

[76] D. Teaney, *Prog. Part. Nucl. Phys.* **62**, 451 (2009).

[77] P. Romatschke, U. Romatschke, *Phys. Rev. Lett.* **99**, 172301 (2007).

[78] G. Policastro, D.T. Son, A.O. Starinets, *Phys. Rev. Lett.* **87**, 081601 (2001).

[79] G. Policastro, D.T. Son, A.O. Starinets, *J. High Energy Phys.* **0209**, 043 (2002).

[80] M. Martinez, M. Strickland, *Nucl. Phys.* **A856**, 68 (2011).

[81] M. Martinez, R. Ryblewski, M. Strickland, *Phys. Rev.* **C85**, 064913 (2012).

[82] W. Florkowski, R. Maj, R. Ryblewski, M. Strickland, *Phys. Rev.* **C87**, 034914 (2013).

[83] W. Florkowski, R. Ryblewski, M. Strickland, *Nucl. Phys.* **A916**, 249 (2013).

[84] D. Bazow, U.W. Heinz, M. Strickland, `arXiv:1311.6720 [nucl-th]`.

[85] M. Strickland, *Nucl. Phys.* **A926**, 92 (2014).

[86] M. Nopoush, R. Ryblewski, M. Strickland, *Phys. Rev.* **C90**, 014908 (2014).

[87] K. Fukushima, F. Gelis, *Nucl. Phys.* **A874**, 108 (2012).

[88] P. Romatschke, R. Venugopalan, *Phys. Rev. Lett.* **96**, 062302 (2006).

[89] P. Romatschke, R. Venugopalan, *Eur. Phys. J.* **A29**, 71 (2006).

[90] P. Romatschke, R. Venugopalan, *Phys. Rev.* **D74**, 045011 (2006).

[91] T.S. Biro, C. Gong, B. Müller, A. Trayanov, *Int. J. Mod. Phys.* **C5**, 113 (1994).

[92] U.W. Heinz *et al.*, *Phys. Rev.* **D55**, 2464 (1997).

[93] J. Bolte, B. Müller, A. Schäfer, *Phys. Rev.* **D61**, 054506 (2000).

[94] H. Fujii, K. Itakura, *Nucl. Phys.* **A809**, 88 (2008).

[95] H. Fujii, K. Itakura, A. Iwazaki, *Nucl. Phys.* **A828**, 178 (2009).

[96] T. Kunihiro *et al.*, *Phys. Rev.* **D82**, 114015 (2010).

[97] S. Mrowczynski, *Phys. Lett.* **B314**, 118 (1993).

[98] S. Mrowczynski, *Phys. Lett.* **B393**, 26 (1997).

[99] A.K. Rebhan, P. Romatschke, M. Strickland, *Phys. Rev. Lett.* **94**, 102303 (2005).

[100] A.K. Rebhan, P. Romatschke, M. Strickland, *J. High Energy Phys.* **0509**, 041 (2005).

[101] S. Mrowczynski, A. Rebhan, M. Strickland, *Phys. Rev.* **D70**, 025004 (2004).

[102] P. Romatschke, M. Strickland, *Phys. Rev.* **D68**, 036004 (2003).

[103] P. Romatschke, M. Strickland, *Phys. Rev.* **D70**, 116006 (2004).

[104] A.K. Rebhan, D. Steineder, *Phys. Rev.* **D81**, 085044 (2010).

[105] A.K. Rebhan, M. Strickland, M. Attems, *Phys. Rev.* **D78**, 045023 (2008).

[106] P. Arnold, J. Lenaghan, G.D. Moore, *J. High Energy Phys.* **0308**, 002 (2003).

[107] P. Arnold, J. Lenaghan, G.D. Moore, L.G. Yaffe, *Phys. Rev. Lett.* **94**, 072302 (2005).

[108] P. Arnold, G.D. Moore, *Phys. Rev.* **D73**, 025013 (2006).

[109] P. Arnold, G.D. Moore, *Phys. Rev.* **D73**, 025006 (2006).

[110] P. Arnold, G.D. Moore, *Phys. Rev.* **D76**, 045009 (2007).

[111] P. Arnold, G.D. Moore, L.G. Yaffe, *Phys. Rev.* **D72**, 054003 (2005).

[112] A. Dumitru, Y. Nara, M. Strickland, *Phys. Rev.* **D75**, 025016 (2007).

[113] D. Bodeker, K. Rummukainen, *J. High Energy Phys.* **0707**, 022 (2007).

[114] J. Berges, D. Gelfand, S. Scheffler, D. Sexty, *Phys. Lett.* **B677**, 210 (2009).

[115] J. Berges, S. Scheffler, D. Sexty, *Phys. Rev.* **D77**, 034504 (2008).

[116] A. Kurkela, G.D. Moore, *J. High Energy Phys.* **1112**, 044 (2011).

[117] A. Kurkela, G.D. Moore, *J. High Energy Phys.* **1111**, 120 (2011).

[118] M. Attems, A. Rebhan, M. Strickland, *Phys. Rev.* **D87**, 025010 (2013).

[119] K. Fukushima, *Phys. Rev.* **C75**, 021902 (2007) [`arXiv:0704.3625 [hep-ph]`] [*Erratum ibid.* **C76**, 021902 (2007)].

[120] K. Dusling, T. Epelbaum, F. Gelis, R. Venugopalan, *Nucl. Phys.* **A850**, 69 (2011).

[121] D. Polarski, A.A. Starobinsky, *Class. Quantum Grav.* **13**, 377 (1996).

[122] D.T. Son, `arXiv:hep-ph/9601377`.

[123] S.Yu. Khlebnikov, I.I. Tkachev, *Phys. Rev. Lett.* **77**, 219 (1996).

[124] R. Micha, I.I. Tkachev, *Phys. Rev.* **D70**, 043538 (2004).

[125] K. Fukushima, F. Gelis, L. McLerran, *Nucl. Phys.* **A786**, 107 (2007).

[126] T. Epelbaum, F. Gelis, *Phys. Rev. Lett.* **111**, 232301 (2013).

[127] J. Berges, K. Boguslavski, S. Schlichting, R. Venugopalan, *Phys. Rev.* **D89**, 074011 (2014).

[128] J. Berges, K. Boguslavski, S. Schlichting, R. Venugopalan, *Phys. Rev.* **D89**, 114007 (2014).

[129] J. Berges, K. Boguslavski, S. Schlichting, R. Venugopalan, *J. High Energy Phys.* **1405**, 054 (2014).

[130] J. Berges, K. Boguslavski, S. Schlichting, R. Venugopalan, `arXiv:1408.1670 [hep-ph]`.

[131] T. Epelbaum, F. Gelis, *Phys. Rev.* **D88**, 085015 (2013).